

## **Towards Silicon-Based Photonic Integrated Circuits: The Quest for Compatible Light Sources**

David J. Lockwood

Measurement Science and Standards, National Research Council Canada,  
Ottawa, Ontario K1A 0R6, Canada

Light emission from silicon and germanium nanostructures has been of great interest for some time now owing to the need for silicon-based light sources for applications in silicon optoelectronics and photonics. Both silicon and germanium possess indirect band gaps, which makes them very inefficient light emitters. Band gap engineering employing quantum wells, wires, or dots has been proposed as one way to overcome this limitation and, in the past, Si/Ge, Si/SiO<sub>2</sub>, or Si/SiGe-alloy thin-multilayer nanostructures grown on Si have been produced on this principle, and although light emission with a greatly improved efficiency has been obtained at low temperatures the emission at room temperature is still very weak, because of exciton dissociation. Recent advances in band gap engineering technology have resulted in the development of different systems incorporating one-, two-, and three-dimensionally confined Si-Ge nanostructures that produce bright light in the visible to near infrared. Here, the novel optical properties of various such nanostructures are reviewed.

### **Introduction**

Light emission from Si and Ge nanostructures (NSs) has been of great interest in recent years (1–4) owing to the need for silicon-based light sources for applications in silicon optoelectronics and photonics (5,6). Optical interconnects are required these days for on-chip technology as an alternative to metal wires, because of data transmission bottlenecks introduced by their unavoidable delay times, significant signal degradation, problems with power dissipation, and electromagnetic interference. Two major avenues toward optical interconnects on a chip include a hybrid approach with III-V densely packaged optoelectronic components and the all-group-IV approach (mainly Si, Ge and SiGe), where all the major components, e.g., light emitters, modulators, waveguides and photodetectors, are monolithically integrated into the CMOS environment (5,6). Both Si and Ge possess indirect band gaps, which makes them very inefficient light emitters (1). Band gap engineering employing quantum wells, quantum wires or quantum dots has been proposed as one way to overcome this limitation and Si/Ge or Si/SiGe-alloy thin multilayer quantum well structures grown on Si have been produced on this principle, and although light emission with greatly improved efficiency has been obtained at low temperatures the emission at room temperature is still very weak, because of exciton dissociation (1,5,7). Recently, through employing novel band-gap engineering strategies, several different entirely new bright light-emitting Si/Ge nanostructures including one

possessing a direct gap have been prepared. The latter structure is based on constructing a new super unit cell comprised of multiple planar epitaxial layers of Si and Ge grown on (001) Si<sub>0.4</sub>Ge<sub>0.6</sub> (8). Others are based on silicon-germanium layers grown epitaxially on silicon in such a way as to form multiple layer three-dimensional nanostructures (quantum dots) (9,10). A simple and efficient electrochemical process that combines galvanic reaction and focused-ion-beam lithography to selectively synthesize gold nanoparticles has been developed that can be used to grow ordered SiGe nanowire arrays with a predefined diameter (200 nm) and position (11,12). Here, the light emitting properties of these and other similar Si/Ge nanostructures that have been found to luminesce efficiently at wavelengths in the important spectral range of 1.1–1.6  $\mu\text{m}$  are compared for their possible use in optoelectronics and photonics. Emphasis is placed on the work carried out at the National Research Council of Canada over the last three decades.

### Optical Evidence for Quantum Confinement Effects in Porous Silicon

Porous silicon (p-Si) was discovered over 60 years ago by Uhlir at Bell Telephone Laboratories, USA (13,14). The porous material is created by electrochemical dissolution in HF-based electrolytes. Hydrofluoric acid, on its own, etches single-crystal Si extremely slowly, at a rate of only nanometers per hour. However, passing an electric current between the acid electrolyte and the Si sample speeds up the process considerably, leaving an array of deep narrow pores that generally run perpendicular to the Si surface. Pores measuring only nanometers across, but micrometers deep, have been achieved under specific etching conditions (15,16). The evenly-spaced pore structure was explained in terms of available paths for the etching current, with each pore surrounded by an insulating layer of material depleted of electrons. After many years of basic research on the chemical and physical properties of p-Si, the formation mechanism of the network of pores is now largely understood and the resulting porous microstructure depends critically not only on the HF acid concentration and anodization parameters (current density or voltage) but also on the type and doping level of the Si crystal (17,18). The Si skeleton left behind has been shown to retain the substrate crystallinity, but with a small lattice expansion compared to bulk Si (19). In the mid-1970s, p-Si was already being considered for use as a dielectric in the development of silicon-on-insulator (SOI) technology for very-large-scale integrated circuits (17,20,21). It is only comparatively recently that the optical characteristics of p-Si have been explored in detail. In 1984, Pickering *et al.* (22) reported on low temperature luminescence in p-Si anodized under a range of conditions and noted a band at higher energy (above the bulk-Si band gap) that shifted up in energy with decreasing p-Si density, but they did not investigate the emission properties at room temperature. The complexities that have arisen in the interpretation of the photoluminescence (PL) were already apparent in this fundamental work.

In July 1989, Canham conceived the idea of fabricating Si quantum wires in p-Si by reverting to the much slower chemical HF etch after the electrochemical etch (23). In this way he proposed to join up the pores leaving behind an irregular array of undulating free standing pillars of crystalline Si (c-Si) only nanometers wide. In 1990, Canham (24) remarkably observed intense visible PL at room temperature in p-Si that had been etched under carefully controlled conditions. Visible luminescence ranging from green to red in color was soon reported by Canham *et al.* for other p-Si samples and ascribed to quantum

size effects in wires of width  $\sim 3$  nm (24,25). Independently, Lehmann and Gösele (26) reported on the optical absorption properties of p-Si. They observed a shift in the bulk Si absorption edge to values as high as 1.76 eV that they also attributed to quantum wire formation. Tremendous activity on research into the physical and associated chemical characteristics of p-Si ensued from these early reports with, unfortunately, some duplication of effort, and a great diversity in their luminescence properties was observed (27). At the National Research Council we quickly joined in this momentous work and from a detailed investigation of the optical properties of p-Si we concluded that there is strong optical absorption evidence for quantum confinement effects in c-Si NSs within p-Si and that the red-orange PL also exhibits a weaker quantum confinement effect (28–33).

Transmission electron microscopy and Raman scattering spectroscopy has shown that in our p-Si samples the porous material is in the form of mainly sphere-like nanocrystals, and thus we refer to the nanostructures as spherites (28). A typical optical transmission curve obtained by at room temperature from a p-Si membrane sample is shown in Fig. 1 together with the corresponding PL spectrum (30). It is very noticeable that the PL peak energy is at a lower energy than the optical absorption edge. This behavior is even more evident when the band gap energy obtained from the optical absorption spectrum is compared for a number of samples of different average diameter, as shown in Fig. 2 (30).

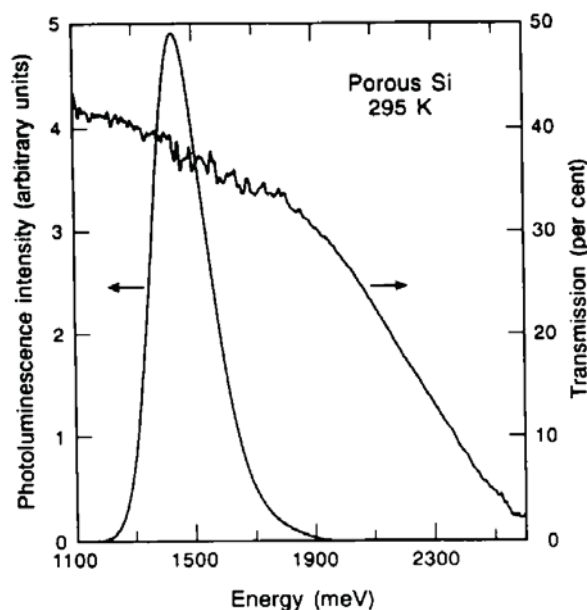


Figure 1. Room temperature transmittance and PL spectra for a p-Si membrane comprised of 3.1 nm spherites.

The PL data in Fig. 2 is in remarkably good agreement with the predictions of simple effective mass theory for quantum dots (28) and this justifies further interpretation within quantum confinement models. A more sophisticated calculation within a linear combination of atomic orbitals (LCAO) framework for c-Si spheres with hydrogen passivated surfaces (34) has predicted a  $d^{-1.39}$  dependence of the optical gap on the sphere diameter,  $d$ . Other calculations for dots (35,36) in a variational envelope function approach produced similar results. The calculated energy gap behavior (34,35) has been shown (27) to be in excellent agreement with optical absorption data for p-Si spherites (29,30,37) and c-Si spheres (38). However, the calculation by Proot *et al.* (25), which is

such a good fit to our absorption data, lies generally above the PL data, as shown in Fig. 2. A similar LCAO calculation has been undertaken for c-Si wires (39) and the predicted energy gap dependence on the wire diameter, which is similar to that obtained from several other theories (27), is also plotted in Fig. 2. The wire theory curve is in closer agreement with the p-Si PL data, as could be expected. However, to permit this more satisfactory comparison with quantum wire theory the extreme and unlikely case of *uniform* wires has to be taken, and thus the energy difference between the absorption and emission data remains unexplained.

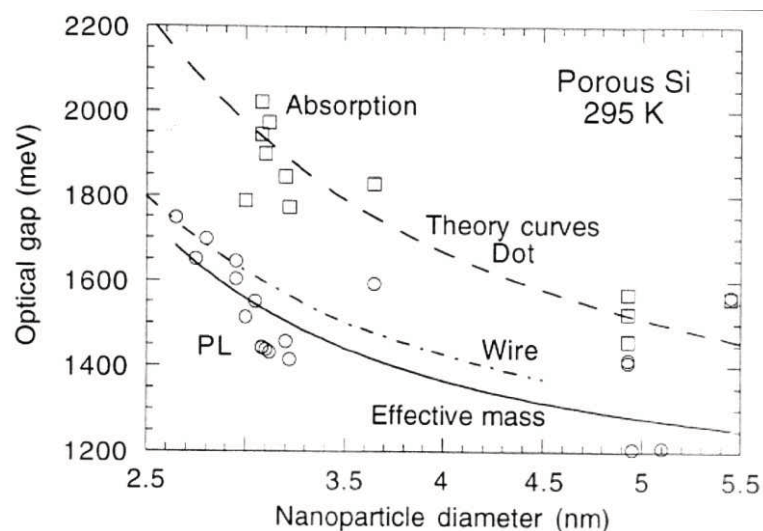


Figure 2. Spherite diameter dependence of the PL peak energy and optical absorption in p-Si samples at room temperature. The solid line is the effective mass model prediction for the optical energy gap in c-Si spheres, while the broken and short dash-dot lines are the theoretical predictions for quantum dots and wires, respectively.

The difference between the predicted energy gap for spheres, as confirmed in our experiments, and the lower energy of the PL peak has to be attributed to the emission mechanism. In the vibronic model, this difference is associated with phonon-assisted transitions employing c-Si phonons of energy  $\sim 65$  meV. The difference between dot theory and experiment evident in Fig. 2 is  $\sim 100$  meV at 5 nm nanoparticle diameter, but it *increases* with decreasing diameter to  $\sim 400$  meV at 3 nm, and is thus incompatible with a vibronic model. That is because in the vibronic model, multiphonon assisted transitions are required where the average number of phonons involved would have to increase with decreasing nanoparticle diameter, which is not normally the case. For our samples, some additional energy loss must occur in the absorption-emission process prior to emission to account for this large difference at small diameters. As the samples have all been treated in the same way after electrochemical etching, we thought at the time that it was unlikely that the blue shift in the PL with decreasing nanoparticle diameter is due to some change in the surface chemistry, and that this would seem to rule out explanations based on surface recombination models. We considered other models such as the formation of bound excitons and the creation of localized excitons due to trapping by donor-like and acceptor-like states (29). It was not until much later that the true cause of the red PL observed in most p-Si samples was identified (40). It was, in fact, related to a specific surface defect in p-Si created by surface oxidation subsequent to drying the sample – new electronic states appear in the band gap of the smaller quantum dots when a Si=O bond is

formed – that produced PL at the observed energy and also exhibited a weak quantum confinement effect. The true intrinsic PL in p-Si is thus only observable when the surface oxidation can be eliminated through effective surface passivation by other methods, such as with Si-H bonds (40) or thermal (non-catalytic) reaction with alkenes and aldehydes (41–46). The latter method leads to high stability (41–46).

Despite this early promise as a room-temperature light emitter, p-Si has not yet been employed as a light emitter in optoelectronics due to the difficulty of integrating it into CMOS production.

### Disordered Silicon Quantum Wells

The simplest approach to investigating quantum confinement effects in Si is to grow well-defined thin quantum wells of Si separated by wide band gap barriers. Suitable barrier candidates are SiO<sub>2</sub>, CaF<sub>2</sub>, and Al<sub>2</sub>O<sub>3</sub> (47), and SiO<sub>2</sub> has the additional advantage of being an excellent passivator of Si (48). Although a number of Si/barrier superlattices have been produced in the past (49) none had produced convincing evidence for quantum confinement induced emission until 1995. In 1995, Lu *et al.* (50) reported visible light emission at room temperature from ultrathin-layer Si/SiO<sub>2</sub> superlattices grown by MBE that exhibited a clear quantum confinement shift with Si layer thickness, as shown in Fig. 3. According to effective mass theory and assuming infinite potential barriers, which is a reasonable approximation since wide-gap (9 eV) 1-nm-thick SiO<sub>2</sub> barriers are used, the energy gap  $E$  for one-dimensionally confined Si should vary as

$$E = E_g + \frac{\pi\hbar^2}{2d^2} \left( \frac{1}{m_e^*} + \frac{1}{m_h^*} \right), \quad [1]$$

where  $E_g$  is the bulk material band gap and  $m_e^*$  and  $m_h^*$  are the electron and hole effective masses (51). This simple model is a reasonable first approximation to compare with experiment for quantum wells (52). The shift in PL peak energy with Si well thickness  $d$  is well represented by Eq. (1), as can be seen in Fig. 3, with  $E(\text{eV}) = 1.60 + 0.72d^2$ . The very thin layers of Si ( $1 < d < 3$  nm) have a disordered (d-Si), but nearly crystalline, structure owing to the growth conditions and the huge strain at the Si–SiO<sub>2</sub> interfaces (53). However, by reducing considerably the SiO<sub>2</sub> thickness below 1 nm, epitaxial growth of the Si layers can be achieved via small holes in the SiO<sub>2</sub> film (54). The fitted  $E_g$  of 1.60 eV is larger than that expected for c-Si (1.12 eV at 295 K), but is in excellent agreement with that of bulk a-Si (1.5–1.6 eV at 295 K). The indications of direct band-to-band recombination were confirmed by measurements via X-ray techniques of the conduction and valence band shifts with layer thickness (50,55). The fitted confinement parameter of 0.72 eV/nm<sup>2</sup> indicates  $m_e^* \approx m_h^* \approx 1$ , comparable to the effective masses of c-Si at room temperature (51). The integrated intensity at first rises sharply with decreasing Si thickness until  $d \approx 1.5$  nm and then decreases again, which is consistent with quantum well exciton emission (56,57). The PL intensity is enhanced by factors of up to 100 upon annealing and is also selectively enhanced and band-width narrowed by incorporation into an optical microcavity (58). In a higher quality cavity, a very sharp (17 meV full width at half maximum) PL peak has been observed (59).

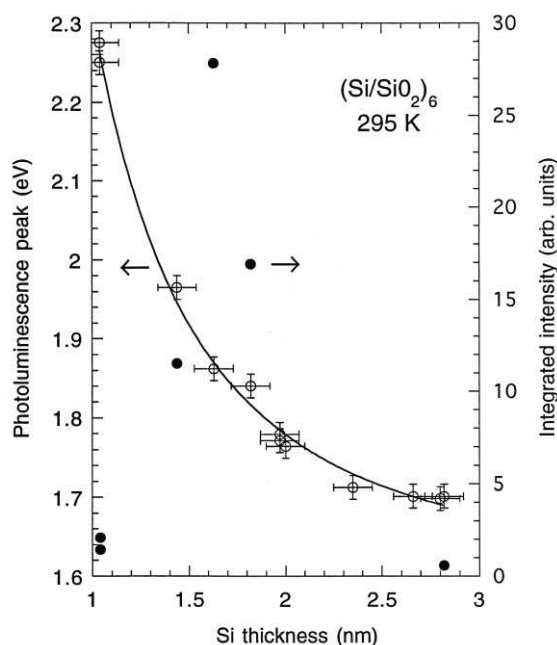


Figure 3. The PL peak energy (open circles) and integrated intensity (full circles) at room temperature in d-Si/a-SiO<sub>2</sub> superlattices as a function of Si layer thickness. The solid line is the fit to the peak energy by effective mass theory.

The bright PL obtained from these and other (60) as-grown and annealed Si/SiO<sub>2</sub> superlattices (see Fig. 4) offers interesting prospects for the fabrication of a Si-based light emitter that can be tuned from 500 to beyond 800 nm by varying the Si-layer thickness and/or the annealing conditions, all using available vacuum deposition technology and standard Si wafer processing techniques. The next important step is to develop LEDs based on such superlattices. Several prototype devices have been constructed in Si/SiO<sub>2</sub> (61–64) and Si/CaF<sub>2</sub> (65) and all report visible EL, although there is no strong evidence that the emission originates from confined states in the Si quantum wells. The EL from the Si/SiO<sub>2</sub> superlattices is notably stable (61,62).



Figure 4. Room temperature PL from a patterned (d-Si/SiO<sub>2</sub>)<sub>100</sub> superlattice, with a periodicity of 2.6 nm, that was post-annealed in air at 1100 °C for 0.5 h. The PL was excited with an Ar laser operating at 457.9 nm and having a power density of ~50 mW/cm<sup>2</sup> at the superlattice surface. The actual size of the logo is ~20×20 mm<sup>2</sup>.

### Crystalline Silicon Quantum Wells

As discussed above, the d-Si/a-SiO<sub>2</sub> system has received the most attention and direct evidence of quantum confinement induced PL has been obtained. However, the as-grown thin Si films (< 3 nm thick) proved very difficult to crystallize by thermal annealing due to strain effects induced by the amorphous SiO<sub>2</sub> (a-SiO<sub>2</sub>) barriers (53,66). In other investigations of single Si quantum-wells formed by the separation by implanted oxygen (SIMOX) process, strong optical recombination of carriers was observed at the c-Si/a-SiO<sub>2</sub> interfaces (67–69) together with selective excitation evidence for a weak intrinsic PL (68). Thus, a detailed experimental study of quantum confinement effects in c-Si/a-SiO<sub>2</sub> had not been possible for ultrathin silicon layers. Such studies are important for comparison with theory, which is incapable at present of predicting the optical properties of quantum confined d-Si. Then in 2002, Lu and Grozea (70) demonstrated the preparation of single nanometer-thick c-Si/a-SiO<sub>2</sub> quantum wells based on oxidizing and etching Canon epitaxial layer transfer (ELTRAN) Si-on-insulator (SOI) wafers. Canon ELTRAN technology uses wafer bonding to fabricate the SOI wafer, which has the benefits of an epitaxial silicon layer that is atomically smooth and free of particles or pits (71). This atomically flat Si/SiO<sub>2</sub> interface is essential for electronic applications of SOI wafers and is the key factor in producing silicon quantum wells only a few atomic layers thick. The SOI wafer has a 200 nm thick buried oxide layer surmounted by a transferred epitaxial (100) Si layer about 50 nm thick. To bring the silicon layer thickness down to a few nanometers, furnace dry oxidation was first used to oxidize the Si layer and thereby reduce the c-Si film thickness to 5–10 nm. To produce c-Si films with a thickness of just a few atomic layers, the film was then thinned down atomic-layer-by-atomic-layer by using a combination of room-temperature UV-ozone oxidation and wet chemical etching, according to the method described in Ref. (70). The resulting c-Si film thickness was determined by X-ray photoelectron spectroscopy (70,72).

Representative results obtained from PL measurements at room temperature of such single wells (73–76) are shown in Fig. 5. The overall intensity of the PL was quite weak, but consistent with a single quantum well as opposed to the multiple well samples discussed above. In general, the overall PL intensity increased at first with decreasing layer thickness and then decreased again (see Fig. 5), much as was observed for d-Si wells, (51) while the overall PL line width increased. The temperature dependence of the PL spectrum (77) of one sample is shown in Fig. 6 and these results are quite revealing. They indicate that the PL envelope actually comprises two bands, one at about 1.79 eV at 4 K and the other at around 1.84 eV. (The differences in PL line shape at 300 K, as compared to the spectrum for the same sample given in Fig. 5, arise from the different responsivities of the two sets of PL equipment.) The two bands do not exhibit strong temperature dependences in their integrated intensities, line widths, or positions, but the 1.8 eV band becomes more evident at lower temperatures. Other samples gave similar results with respect to the temperature dependences of the band parameters and also indicated the presence of two bands. The PL line shape could be readily curve-resolved into two bands, as shown in Fig. 5. The presence of these two overlapping bands explains the apparent overall PL intensity and linewidth variation with Si layer thickness.

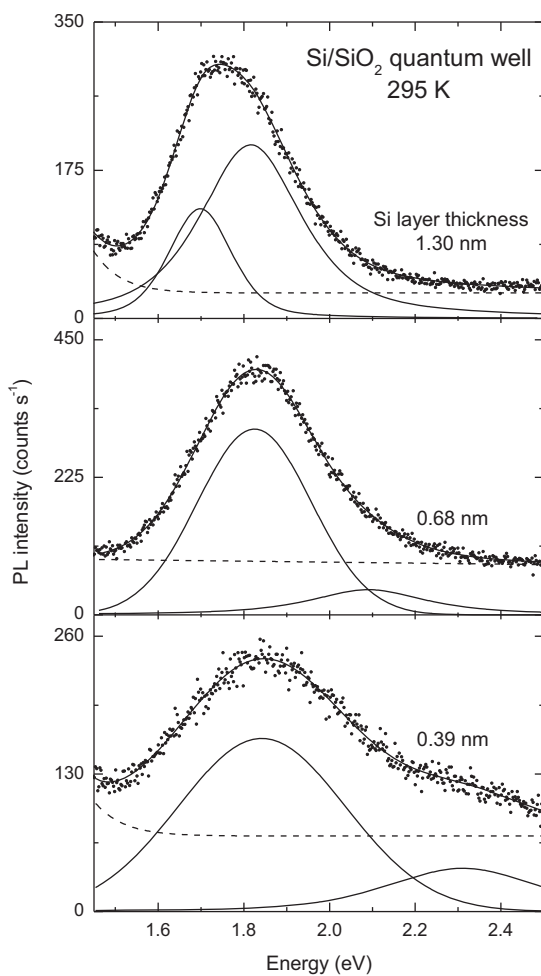


Figure 5. Room temperature PL from single c-Si/a-SiO<sub>2</sub> quantum wells of different thickness. The PL line shape has been fitted with the two bands (indicated by the solid line passing through the data points) shown below by the solid lines. The dashed line is the fitted background.

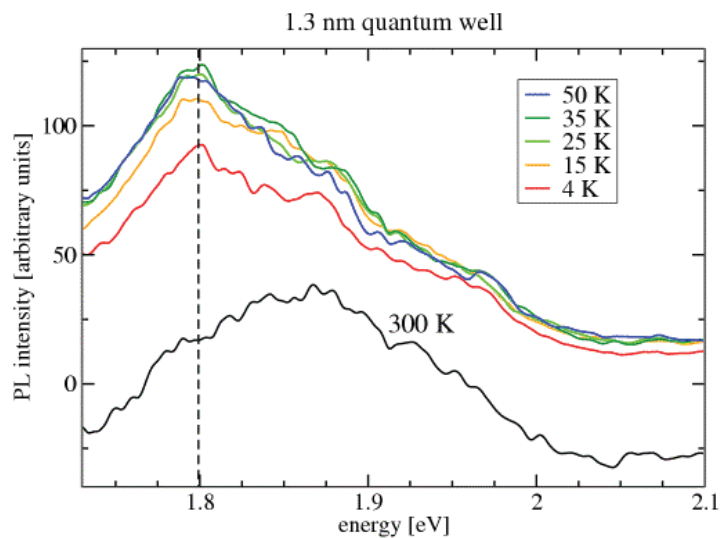


Figure 6. Temperature dependence of the PL from a 1.3 nm thick single c-Si/a-SiO<sub>2</sub> quantum well.

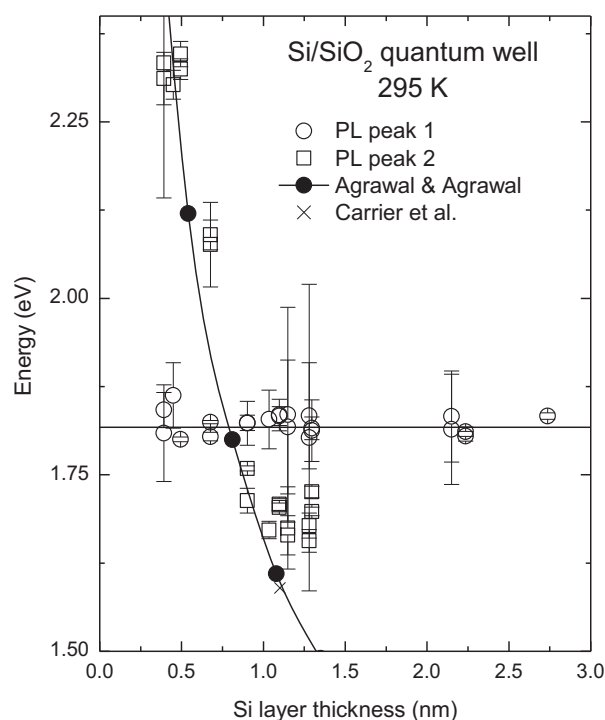


Figure 7. Experimental results ( $\circ, \square$ ) for the energies of the two PL bands of single c-Si/a-SiO<sub>2</sub> quantum wells as a function of well thickness compared with the theory of Agrawal and Agrawal ( $\bullet$ ) (78) and Carrier *et al.* ( $\times$ ) (79). The solid line is an interpolation of the theoretical data. The error bars represent the standard deviation in the peak energy determined from the fits. The horizontal solid line is a least-squares fit to the data of peak number 1.

The fitted PL band energies as a function of c-Si layer thickness are plotted in Fig. 7. The energy of peak number 1 scarcely varies with Si layer thickness, while peak number 2 exhibits a strong dependence on this thickness. The second band could not be detected for samples with layer thicknesses greater than 1.3 nm, including one sample with a layer thickness of 4.26 nm. This would imply that the band peak energy was lower than the instrumental detection limit of 1.45 eV. The band gap energy variation predicted from theoretical calculations based on self-consistent full potential linear muffin-tin orbital (78) and first-principles projector-augmented wave (79) methods are also shown in Fig. 6. These calculations take into account properly the layered structure (78,79), the SiO<sub>2</sub> barriers (79), and the strained c-Si/c-SiO<sub>2</sub> interface (79) and differ from the predictions of earlier theoretical models that have relied mostly on a simple H-termination of an isolated Si nanocluster (80,81). In these theories, the band gap energy is that of bulk c-Si (1.1 eV) in the limit of ultrawide quantum wells, which contrasts with that of d-Si (1.6 eV). The experimental results for peak 2 are in remarkable agreement with theory, confirming the origin of this peak as intrinsic quantum-well emission from c-Si and validating the theories. The strong dependence on Si layer thickness evident for thicknesses less than 1.5 nm indicates why peak number 2 was not observed experimentally for larger layer thicknesses ( $> 2$  nm) due to the cut-off in the instrumental response. The higher energy gaps,  $E_1$  and  $E_2$ , of c-Si were also investigated by spectroscopic ellipsometry for these samples, but contrary to the fundamental band gap behavior no significant variation with well thickness was observed (82).

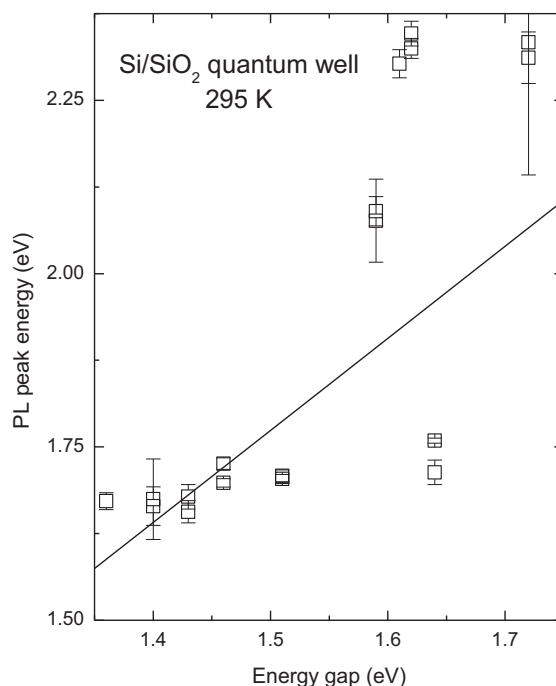


Figure 8. Energy of PL peak number 2 versus the measured energy gap for single c-Si/a-SiO<sub>2</sub> quantum wells. The straight line is an error-weighted least-squares fit to the data.

The experimental energy gap for these samples has been determined previously by X-ray techniques, as reported in Ref. 70. The PL energy of peak number 2 increases in accord with the increasing energy gap with decreasing Si layer thickness, as shown in Fig. 8 (75). A least-squares error-weighted linear fit to the data yielded a zero intercept of  $-0.2 \pm 0.8$  and a slope of  $1.3 \pm 0.5$  for the relationship between the PL and band-gap energies. This, within error, is the direct proportionality expected for true quantum confinement induced PL (50,83). Thus these experimental results provide the first verification of such theories and vindicate the approaches taken and their associated approximations. These theories can now be applied with confidence to enumerating other properties of the c-Si/SiO<sub>2</sub> system and analogous structures.

The data for peak number 1 in Fig. 7 are a good fit to a constant energy of 1.82 eV. Such a behavior negates assignment to light emission within the quantum well. Experimental studies of carrier recombination in oxidized silicon nanostructures have shown similar weak trends with change in Si nanocrystal size (84). In particular Wolkin *et al.* (40) observed a dramatic drop in the confined PL energy for small Si dot diameters ( $< 2$  nm) when the silicon was oxidized and attributed this red shift to recombination involving a trapped electron or exciton. By analogy with these results and others where a PL peak near 1.8 eV is commonly observed (27,84), the PL mechanism in our samples is similarly attributed to trapped state emission at the c-Si/a-SiO<sub>2</sub> interface. This mechanism would account for the observed very weak confinement effect on peak number 1.

Subsequent work by Cho *et al.* (69) has confirmed the observation of quantum confinement induced PL from c-Si/a-SiO<sub>2</sub> wells produced by high temperature thermal oxidation of ELTRAN SOI wafers, but in this case weak or no interface mediated PL was seen. Most remarkably, stimulated emission from such a single c-Si/a-SiO<sub>2</sub> quantum well

has been observed by Saito *et al.* (85,86) using electrical pumping in a device constructed entirely with conventional CMOS technology, but so far no lasing action has been reported.

### Super Unit Cell

In recent times, through employing novel band gap engineering computations, entirely new Si/Ge (87) and Si (88) structures possessing direct gaps have been proposed. The former structure is based on constructing a new super unit cell comprised of multiple epitaxial layers of Si and Ge grown on (001)  $\text{Si}_{1-x}\text{Ge}_x$  with  $x \geq 0.6$  (87) while the latter structure comprises a metastable cubic  $\text{Si}_{20}$  phase with a quasi-direct band gap of 1.55 eV (88). According to d'Avezac *et al.* (87), a  $\text{SiGe}_2\text{Si}_2\text{Ge}_2\text{SiGe}_n$  superstructure on  $\text{Si}_{0.4}\text{Ge}_{0.6}$  should have a direct and dipole-allowed gap of 0.863 eV, which is ideally suited for optical fiber data transmission applications.

To investigate the first proposal, two similar samples have been prepared by quite different growth methods: molecular beam epitaxy (MBE) and solid phase epitaxy (SPE). In both samples the  $\text{SiGe}_2\text{Si}_2\text{Ge}_2\text{SiGe}_{12}$  superstructure was grown on a 5  $\mu\text{m}$  thick relaxed buffer layer of  $\text{Si}_{0.4}\text{Ge}_{0.6}$  on a 750  $\mu\text{m}$  thick (001) Si substrate (8,89).

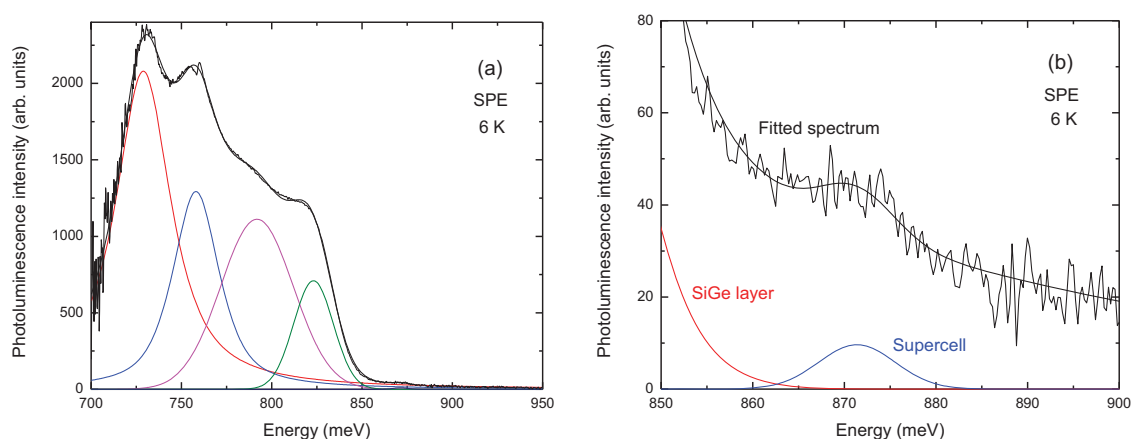


Figure 9. (a) Curve-resolved PL spectrum of the SPE-grown sample at 6 K obtained with 405 nm excitation. (b) Curve-resolving results obtained near the 871-meV PL peak. The solid line shows the fit to the PL data, while component lines are shown underneath.

Characteristic PL results, as obtained for the SPE-grown sample at 6 K, are shown in Fig. 9. Four strong peaks are seen at 728.9, 758.1, 791.8, and 823.1 meV and a much weaker peak at 871.4 meV [Fig. 9(b)]. A fit to the PL results obtained from the same sample at 20 K yielded strong peaks at 724.2, 756.5, 781.6, and 812.6 meV and a weak peak at 869.1 meV. Similar results were obtained from fits to the MBE-grown sample spectra, which were less intense (8,89).

Given the quite close agreement in energy, the weak peak at 0.871 eV is the expected dipole-allowed direct-gap transition predicted to be at 0.863 eV in the superstructure. This peak can be anticipated to be quite weak in PL owing to the fact that this composite layered structure in our samples is only one ‘unit cell’ thick. Apart from the uncertainty arising from the standard error in the fits ( $\sim 4$  meV), the remaining small difference in energy between theory and experiment could easily be the result of a difference in strain

within the layer in the sample compared with the ideal (perfect) modeled structure or arise from assumptions made for parameter values in the model.

Because of their high intensity, the other four peaks must arise from the  $\text{Si}_{0.4}\text{Ge}_{0.6}$  relaxed buffer layer, which is the thickest component of the structure apart from the Si substrate itself that contributes only very weakly to the PL. The energies of the peaks, however, are much lower than that expected for a bulk  $\text{Si}_{0.4}\text{Ge}_{0.6}$  alloy where the indirect energy gap is 971 meV (90). The energy separations and general appearance of these peaks is reminiscent of PL that has been attributed to the presence of various dislocation defects (i.e., the four so-called D-lines) in Si (91–94) and SiGe alloys (91). These PL features are quite sharp in Si (91,92), but are much broader in higher Ge-concentration alloys (95). It is therefore most likely that this PL arises predominately from dislocations formed during the growth of the relaxed alloy buffer layer on the Si substrate.

In summary, experimental evidence has been obtained of the predicted direct-gap optically-allowed transition in a specially engineered supercell comprised of a number of ultrathin layers of Si and Ge. For two quite differently prepared samples, a peak is observed at 0.871 eV, which is very close in energy to the theoretically predicted direct gap of 0.863 eV for this particular structure. Unfortunately, from a room temperature device point of view, the peak is only observable presently at low temperatures ( $< 25$  K).

### Three-Dimensional SiGe Nanostructures

An overview of earlier work on light emission from SiGe nanostructures in general, including quantum wells, wires, and dots, has been given elsewhere (96). Here, we provide an overview of recent continuous-wave (CW) and time-resolved PL investigations of the recombination dynamics of three-dimensional (3D) Si/Si<sub>1-x</sub>Ge<sub>x</sub> multilayer nanostructures grown by MBE (9,10). The measurements were performed on Si/Si<sub>1-x</sub>Ge<sub>x</sub> nanostructures where a single Si<sub>1-x</sub>Ge<sub>x</sub> nanometer-thick layer (NL) is incorporated into Si/Si<sub>0.6</sub>Ge<sub>0.4</sub> 3D-cluster multilayer (CM) structures.

#### Wavy Nanolayer

Figure 10(a) shows a dark field transmission electron microscope (TEM) image and spatial position of an energy-dispersive X-ray spectroscopy (EDX) scan for the two Si/SiGe cluster layers closest to the Si-substrate of a multilayer structure [see Ref. (9) and references therein]. The EDX data show that the Ge atomic concentration at a Si/SiGe hetero-interface increases from 0 to ~35 at. % within a distance  $d \approx 5$  nm [Fig. 10(b)]. In contrast, Fig. 11 shows corresponding data for the two top Si/SiGe clusters layers, where the Ge atomic concentration reaches ~35 at. % within a much shorter distance  $d \approx 3$  nm. It is very clear that the topmost Si/SiGe cluster layers in this specially engineered sample (note the increased thickness of the second-to-top layer) have more abrupt Si/SiGe hetero-interfaces compared to those in bottom layers, closer to the Si substrate.

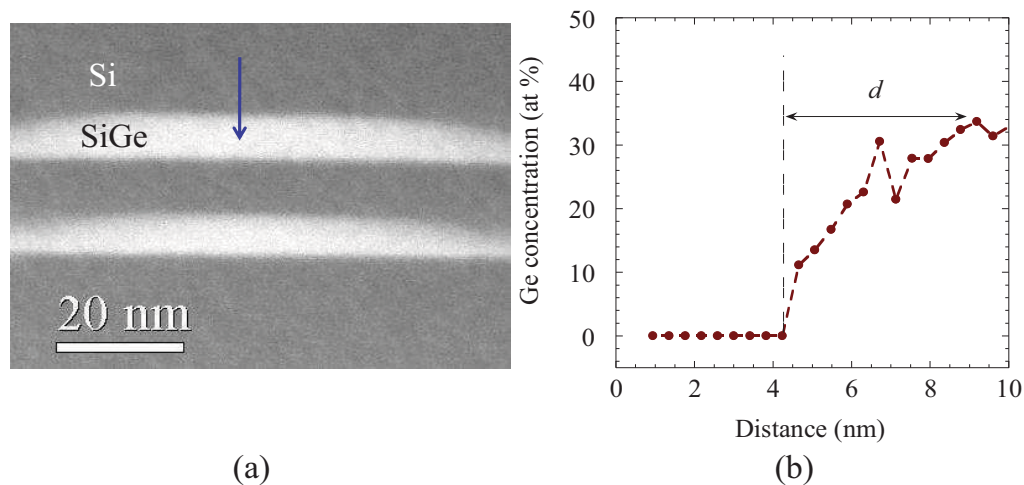


Figure 10. (a) A high angle annular dark field scanning transmission electron microscope (HAADF-STEM) micrograph showing the 1<sup>st</sup> and 2<sup>nd</sup> bottom SiGe cluster layers (counting from the Si substrate) and EDX scan position (arrow). (b) EDX measured Ge atomic concentration at the 2<sup>nd</sup> bottom Si/SiGe cluster layer hetero-interface. The interface abruptness  $d$  (which is the distance between pure Si and SiGe with the nominal Ge-concentration) is indicated.

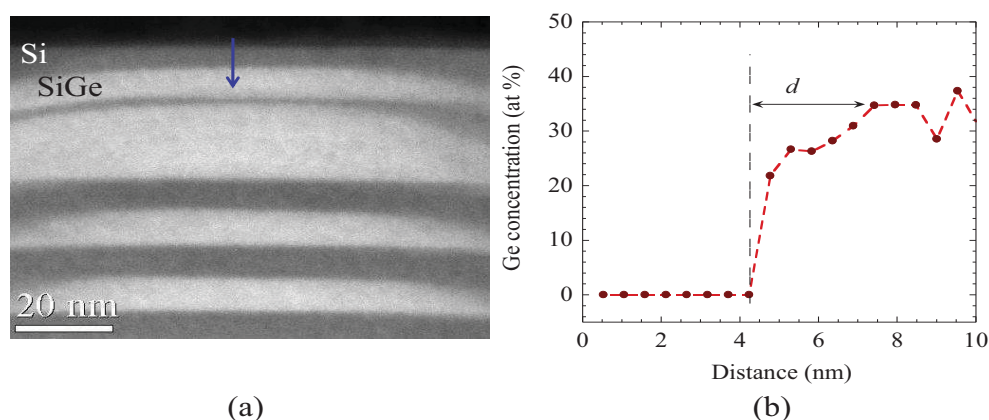


Figure 11. (a) A HAADF-STEM micrograph showing top SiGe cluster layers and EDX scan position (arrow). (b) EDX measured Ge atomic concentration at the topmost Si/SiGe cluster layer hetero-interface. The interface abruptness  $d$  is indicated.

The PL spectroscopy measurements [see Fig. 12(a)] are consistent with the TEM and EDX data. Using photoexcitation of 405 nm wavelength (which has a penetration depth of  $\sim 100$  nm), we observe a PL spectrum with a full width at half maximum (FWHM) of  $\sim 130$  meV. At the same time, using photoexcitation with a wavelength of 325 nm (with an estimated penetration depth of  $\sim 10$  nm), we find the PL spectrum slightly shifted to lower photon energy and with a significantly reduced FWHM ( $\sim 100$  meV). This result clearly indicates that SiGe cluster composition and Si/SiGe interface abruptness (Figs. 10 and 11) are also reflected in the PL spectra: in top-most SiGe layers, a higher Ge-composition results in the PL peak shifted toward lower photon energy, and the more abrupt Si/SiGe interface is responsible for the reduced FWHM of the PL peak (97).

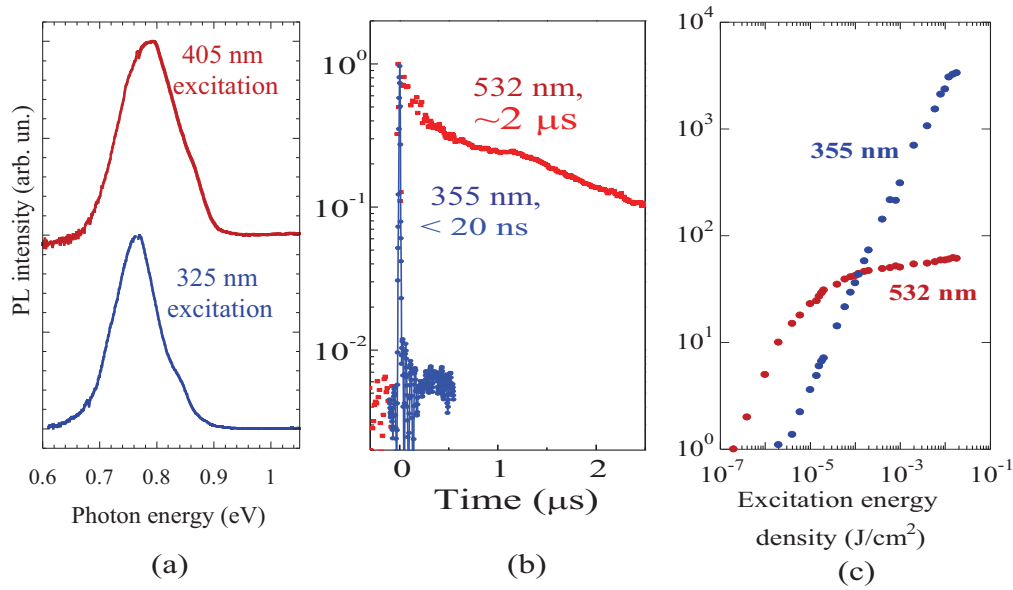


Figure 12. (a) Normalized PL spectra (shifted for clarity) collected at different (indicated) excitation wavelengths. (b) PL decays measured at 0.78 eV under  $\sim 6$  ns duration pulsed excitation at the wavelengths indicated. (c) PL intensity as a function of excitation energy density at different excitation wavelengths. The sample temperature was 15 K.

Figures 12(b) and (c) compare PL lifetimes and PL intensity as a function of excitation energy density measured under pulsed laser excitation with a pulse duration of  $\sim 6$  ns. We find that PL excited at 532 nm and recorded at 0.78 eV (which originates from the lowermost Si/SiGe cluster layers) has a lifetime approximately 100 times longer compared to the same PL excited using 355 nm (PL from the topmost Si/SiGe cluster layers). The PL lifetime for 3D SiGe nanostructures is less than 20 ns, and it is independent of excitation energy density until a very high level of excitation. With the PL decays produced under 355 nm excitation where the energy density varied from  $10^{-5}$  to  $5 \times 10^{-2} \text{ J}/\text{cm}^2$ , no changes in the PL lifetime are found until the Auger limit has been reached, with a carrier concentration approaching  $\sim 10^{19} \text{ cm}^{-3}$  [see Fig. 12(c) and Ref. (98)]. On the contrary, the PL decay under 532 nm excitation quickens while the PL intensity saturates as a function of excitation energy density. Also, we find a dramatic difference in the PL intensity as a function of excitation energy density for excitation at different wavelengths: the PL intensity under 532 nm excitation quickly saturates [in agreement with Refs. (98) and (99)], while under 355 nm excitation the PL intensity is linear versus excitation intensity for many orders of magnitude [Fig. 12(c)].

The results presented here clearly demonstrate that in Si/SiGe 3D nanostructures the PL peaked near 0.78 eV strongly depends on the Si/SiGe hetero-interface abruptness. Our measurements show that in MBE-grown low defect density 3D Si/SiGe nanostructures a transition from pure Si to  $\text{Si}_{1-x}\text{Ge}_x$  with  $x \approx 0.3-0.4$  may require an interface width of more than 5 nm. These diffused type II Si/SiGe hetero-interfaces are responsible for significant ( $d > 5$  nm) electron-hole spatial separation and slow PL, which cannot compete with Auger recombination even at low excitation intensities. However, by engineering more abrupt Si/SiGe hetero-interfaces with  $d \approx 3$  nm, we find a PL lifetime of  $< 20$  ns, which is only a little longer than that found in direct band-gap III-V semiconductors. This extremely fast PL has a quite high quantum efficiency, which, in

contrast to previously reported results from similar nanostructures, remains constant over many orders of magnitude of excitation intensity.

### Planar Nanolayer

Figure 13(a) shows a TEM image of the sample structure, which consists of a Si substrate (not shown in the figure), a  $\text{Si}_{1-x}\text{Ge}_x$  buffer layer with  $x \approx 10$  at. % (seen in part at the bottom of the figure), eight repeats of  $\text{Si}_{1-x}\text{Ge}_x$  cluster (up to 10 nm thick) and Si layer pairs, a single 4-5 nm thick  $\text{Si}_{1-x}\text{Ge}_x$  planar NL followed by a thin Si layer, and a final  $\text{Si}_{1-x}\text{Ge}_x$  cluster layer topped with a Si capping layer (9). The size of the SiGe clusters and thickness of the NL obtained from the TEM measurements is confirmed by EDX measurements, as shown in Fig. 13(b). Also, the EDX scan shows that the  $\text{Si}_{1-x}\text{Ge}_x$  NL composition is relatively uniform with  $x \approx$  at. 8%, while in the  $\text{Si}_{1-x}\text{Ge}_x$  clusters  $x$  increases from  $\sim 5$  at. % at the SiGe cluster/Si interface to 40 at. % near the cluster center.

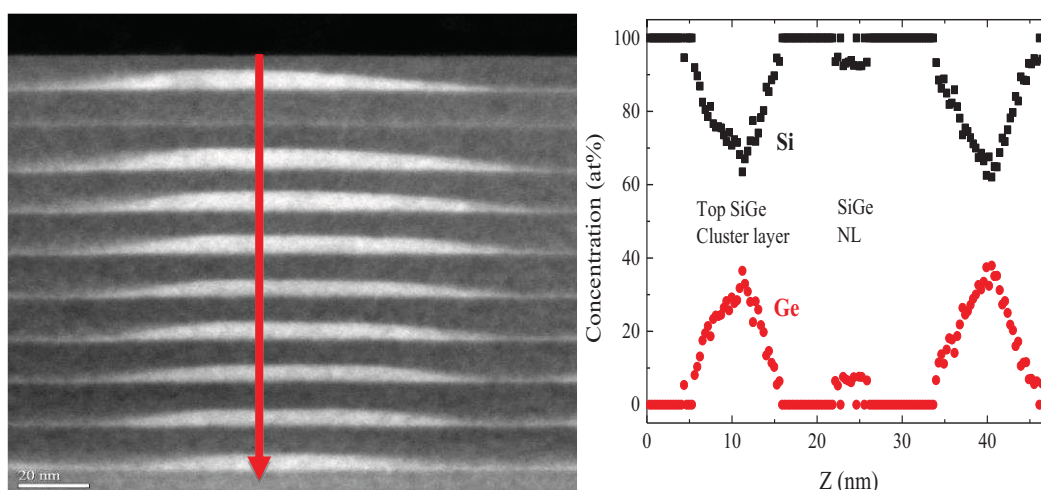


Figure 13. (a) HAADF-STEM image showing the Si/  $\text{Si}_{1-x}\text{Ge}_x$  NL/CM nanostructure with the very thin  $\text{Si}_{1-x}\text{Ge}_x$  NL fourth from the top (Si) layer, and (b) EDX measured composition of the sample's six topmost layers. The arrow shows the direction of the EDX scan. The scale bar in the TEM image is 20 nm in length.

Figure 14(a) compares the PL dynamics associated with  $\text{Si}_{1-x}\text{Ge}_x$  NL and  $\text{Si}_{1-x}\text{Ge}_x$  clusters using 355-nm wavelength and 6-ns duration pulsed-laser excitation with an energy density of  $\sim 50$  mJ/cm<sup>2</sup>. Nanolayer PL from the sample peaked at 0.92 eV and rises faster than the system time resolution, while CM PL, which peaked at 0.8 eV, has a rise time close to 2–3  $\mu$ s. Analogous to the wavy layer case, the PL peaked at 0.92 eV is also found to be decaying much faster compared to the PL peaked at 0.8 eV. Non-exponential decays are found for both PL bands of the Si/SiGe CMs. The observed non-exponential PL decays suggest that in both cases the carrier recombination processes are characterized by a time-dependent recombination rate,  $R_i$ . Figure 14(b) presents the recombination rate extracted from the PL decay data as a function of time. The recombination rate for the PL band peaked at 0.8 eV is  $\sim 10^5$ – $10^4$  s<sup>-1</sup>, and it is in the range of  $10^6$ – $10^7$  s<sup>-1</sup> for the 0.92 eV band.

At a higher excitation energy density, the PL peaked at 0.92 eV dominates due to the PL intensity linear dependence versus excitation energy density compared to the sub-

linear dependence of the 0.8 eV peaked PL, just like in the wavy layer case. The linear dependence of the 0.92 eV peaked PL intensity versus excitation energy density indicates that the measured recombination rate of  $10^6$ – $10^7$  s $^{-1}$  is mostly due to radiative recombination. Since radiative recombination competes with Auger recombination, the long-lived PL should saturate sooner compared to the short-lived PL. On the other hand, the 0.8 eV PL rise time as a function of excitation energy density shows different behavior at low and high excitation energy densities (10). The observed PL rise time of  $\sim 2$ – $3$   $\mu$ s is much longer than the laser pulse ( $\sim 6$  ns). This unusually long PL rise time could be associated with an Auger-assisted carrier spatial redistribution in Si/SiGe nanostructures known as the Auger fountain (100). The temperature dependence of the PL rise time at high excitation density ( $\sim 50$  mJ/cm $^2$ ) also confirms that the Auger fountain could be responsible for the unusual PL dynamics (101).

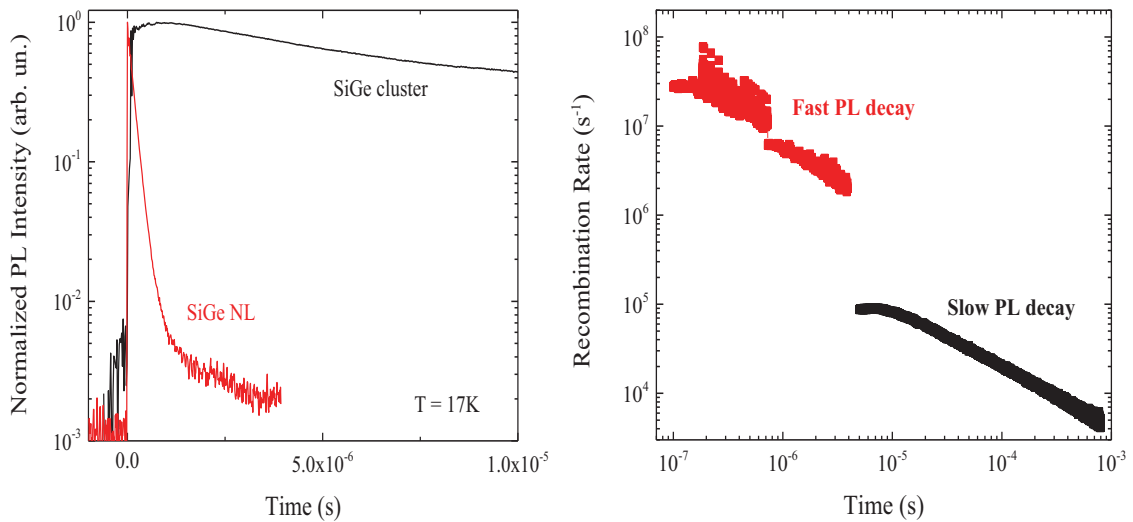


Figure 14. (a) Low temperature (17 K) time-resolved PL decays under pulsed excitation energy density of 50 mJ/cm $^2$  recorded at photon energies associated with Si $_{1-x}$ Ge $_x$  NL PL ( $\sim 0.92$  eV) and Si $_{1-x}$ Ge $_x$  cluster PL ( $\sim 0.8$  eV). (b) Carrier recombination rate as a function of time calculated using the PL decay data. The fast and slow PL decays are from the NL and clusters, respectively.

Non-exponential PL decays have been reported previously in Si/SiGe NSs, and they were fitted variously by a stretched exponential function  $\exp[-(t/\tau)^\beta]$ , a power function  $1/(1 + \alpha t)^m$ , or multiple exponential decays (98,102,103); however, the underlying physical mechanism involved has not been identified. It has been pointed that the stretched exponential PL decay is observed in a wide variety of systems and although it provides a good empirical fit, it most likely has no fundamental significance (104). Instead, we extract the recombination rate directly from the PL decays without using any assumption or a specific model. Figure 14(b) shows that initially both PL bands have almost time-independent recombination rates with corresponding single-exponential decays of  $\sim 3 \times 10^7$  s $^{-1}$  for the PL band peaked at 0.92 eV and  $\sim 9 \times 10^4$  s $^{-1}$  for the 0.8 eV PL band (most likely due to the limited system time resolution). As time increases, the recombination rate decreases, and  $R_i(t) \sim t^{-\alpha}$  with  $\alpha \approx 0.82$  for the PL band peaked at 0.92 eV and  $\alpha \approx 0.67$  for the PL band peaked at 0.8 eV.

We assume that the holes are localized within SiGe and the electrons are located in Si, which is due to the type II energy band alignment at the Si/ Si<sub>1-x</sub>Ge<sub>x</sub> hetero-interface. Just as in the donor-acceptor pair (DAP) recombination model (105), we explain the electron-hole time-dependent recombination rate by assuming that it depends on the average distance separating electrons and holes,  $a_{e-h}$ . The recombination-rate distance dependence is expressed as

$$R(a) = R_0 \exp\left(-\frac{a_{e-h}}{a_0}\right) \quad [2]$$

where  $R_0$  and  $a_{e-h}$  are the maximum recombination rate [ $\sim 10^8$  s<sup>-1</sup>, see Fig. 14(b)] and a minimal radius of the localized exciton at the Si/ Si<sub>1-x</sub>Ge<sub>x</sub> hetero-interface ( $\sim 1.5$  nm), respectively. In the Si<sub>1-x</sub>Ge<sub>x</sub> NL with  $x \sim 8$  at. %, we find  $a_{e-h} \leq 5$  nm (which is comparable to the thickness of the Si<sub>1-x</sub>Ge<sub>x</sub> NL) while in Si<sub>1-x</sub>Ge<sub>x</sub> CMs with  $0 \leq x \leq 40$  at. %, we find  $9 \text{ nm} < a_{e-h} < 14$  nm (Fig. 15). These results are in good agreement with the TEM and EDX data (see Fig. 13).

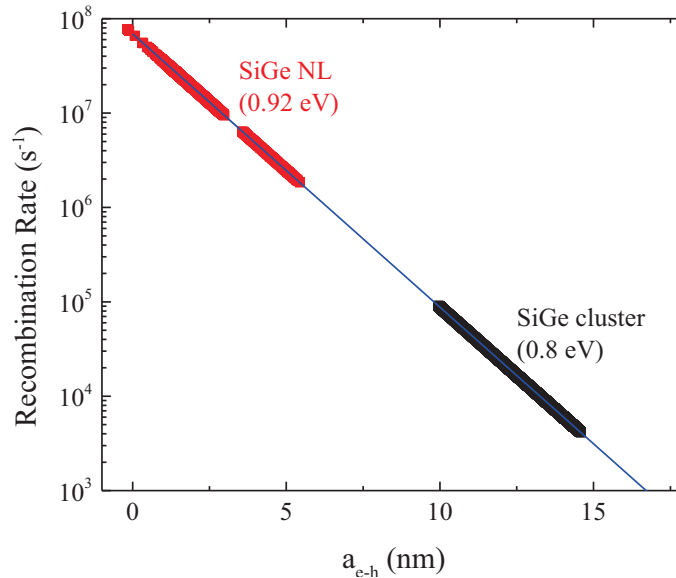


Figure 15. Carrier recombination rates (dots) extracted from the experimental data as a function of the distance between electrons and holes for photon detection energies associated with Si<sub>1-x</sub>Ge<sub>x</sub> NL PL ( $\sim 0.92$  eV) and Si<sub>1-x</sub>Ge<sub>x</sub> cluster PL ( $\sim 0.8$  eV). The solid line is the theoretically calculated electron-hole recombination rate.

In summary, these experiments have shown that two quite different Si<sub>1-x</sub>Ge<sub>x</sub> NLs incorporated into a Si<sub>0.6</sub>Ge<sub>0.4</sub> CM structure exhibit an intense PL signal with a characteristic decay time as much as 1000 times shorter than that observed in Si/SiGe CMs. The experimentally observed non-exponential PL decays in Si/SiGe nanostructures can be explained as being due to variations of the distances separating electrons and holes at the Si/SiGe hetero-interface. It is seen that an abrupt Si/Si<sub>1-x</sub>Ge<sub>x</sub> hetero-interface reduces the carrier radiative recombination lifetime and increases the PL quantum efficiency, making these Si<sub>1-x</sub>Ge<sub>x</sub> NL/CM nanostructures promising candidates for applications in CMOS compatible light-emitting devices.

### SiGe Nanowire Arrays

Semiconductor nanowires (NWs) are thought of as promising building blocks for opto-electronic devices that exploit their novel electronic band structures generated by two-dimensional (2D) quantum confinement in conjunction with their associated optical properties (106–108). However, in order to fully implement these new properties, strict control is needed over the NW location, uniformity, composition, and size. Many of the existing NW growth methods have led to NWs possessing non-uniform diameters and lengths and that are haphazardly oriented and randomly positioned (109). An efficient and simple electrochemical process has been developed that combines focused-ion-beam (FIB) lithography and galvanic reaction to selectively synthesize gold nanoparticles in well-defined locations that are subsequently used for the MBE growth of ordered  $\text{Si}_{1-x}\text{Ge}_x$  NW arrays with predefined NW positions and diameters (11), as shown for example in Fig. 16. Here we summarize the optical properties of such MBE-grown well-ordered NWs.

Three NW samples were prepared for this study (11): Sample (A), where the NWs are grown randomly across the Si substrate; sample (B), where the nanowires decorate the edges of  $400 \times 400 \mu\text{m}^2$  boxes; and sample (C), where the NWs fill  $400 \times 400 \mu\text{m}^2$  boxes in ordered arrays, as described above. These samples have NWs that have a nominal Ge concentration of  $x = 0.15$  and are 200 nm in diameter and 200 nm long, with a morphology similar to the Si NWs shown in Fig. 16.

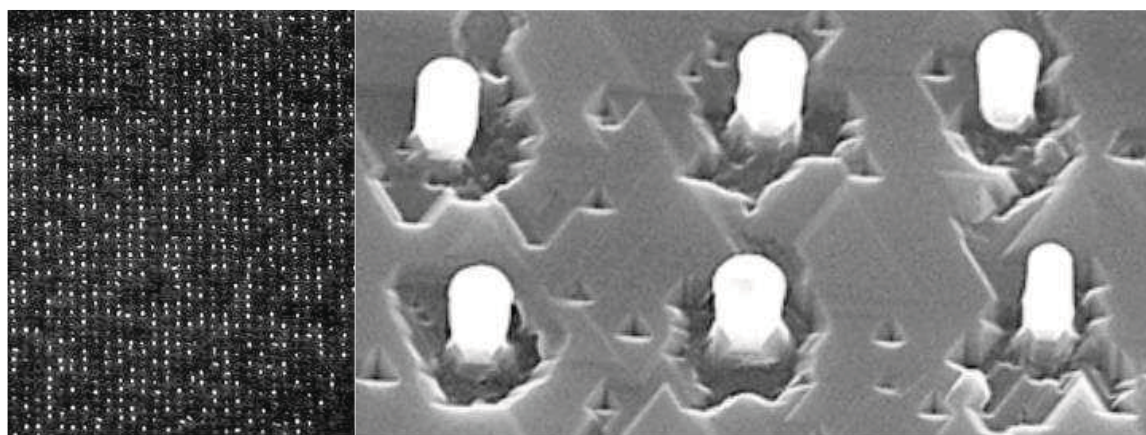


Figure 16. Scanning electron microscope (SEM) images of the ordered arrays of Si NWs showing (left) a NW array and (right) individual 200 nm long NWs.

The temperature dependence of the PL spectrum obtained from sample (C) is shown in Fig. 17. PL spectra with similar temperature dependences were obtained from the other samples. Figure 17 shows that the NW spectral region of interest (from approximately 950 to 1050 meV) is dominated by the boron ( $\sim 10^{17} \text{ cm}^{-3}$ ) doped Si-substrate phonon-replica spectrum at the lowest temperatures (6 and 10 K). Upon increasing the sample temperature up to 20 K, the Si-substrate PL becomes sufficiently quenched from the increasing dissociation of multiple-donor bound excitons within the substrate (110) such that the underlying NW PL is more readily seen. By 25 K, only one sharp line at 1092.5 meV due to the Si substrate remains. Although their spectra were quite similar, the overall intensity of the NW PL varied from sample to sample; sample (C), with a higher

density of NWs distributed within the array, was the strongest, while sample (A) with a random distribution of NWs was the weakest.

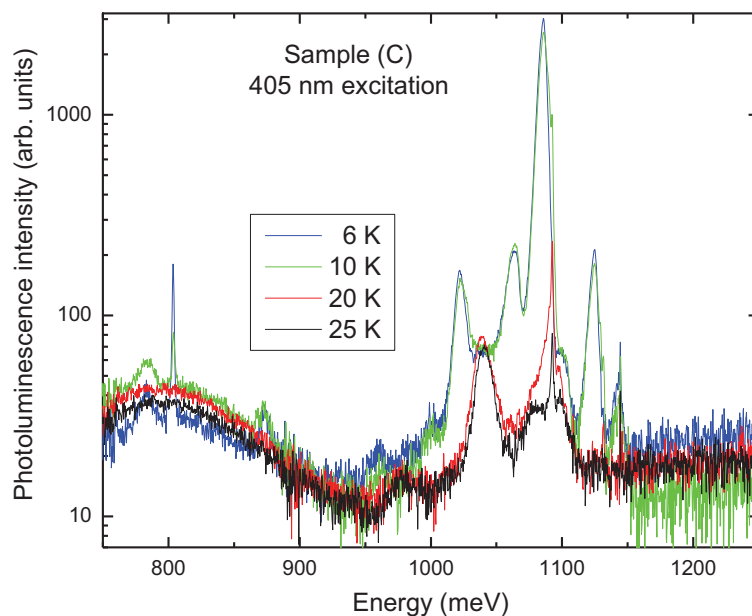


Figure 17. Temperature dependence of the instrument-response-corrected PL spectrum obtained from sample (C) with excitation at 405 nm.

The NW PL is strong considering that the volume of NW material is so small (each wire has a volume of  $0.006 \mu\text{m}^3$ ) and thus the carriers have to be recombining efficiently within the wires to produce this level of light emission at the SiGe-alloy band gap energy. We know from earlier studies of SiGe etched wires (111) and dots (96) that just the spatial confinement of carriers is sufficient to produce the readily-observed PL found here. This implies that the carriers in these samples are not being lost in large numbers to the substrate or recombining in large quantities at defects inside or on the surface of the NWs. The wires are too large in diameter for a quantum confinement induced energy shift in the band gap, but the phonon energies could be affected slightly by confinement and surface effects (112). The wires are grown free-standing and thus there should be no internal strain (i.e., bulk-like energy values should be observed).

Further details about the PL spectra can be obtained from spectral curve resolving. Such an analysis using a Gaussian line shape revealed that there are four major features in the energy range of interest (see Fig. 18 for typical results obtained at 25 K). In order of increasing energy, they are readily assigned to the NW free-exciton transverse-optic (TO) Si-Si vibrational mode, NW free-exciton transverse-acoustic (TA) phonon, Si-substrate-bound-exciton TO phonon and NW free-exciton no-phonon (NP) lines, respectively (90,110). The amplitude ratio for the TO/TA peaks is much the same in the three samples, as would be expected if both lines arose just from the NWs and that the NWs were of similar composition in all samples. The fitted frequencies and line widths for the respective NW and Si TO mode lines are the same within error. Interestingly, the free-exciton NP line intensity relative to its phonon replicas (TA and TO lines) in these NWs is much more intense than that found in bulk Si, but is somewhat lower compared to what is observed in bulk alloy material of a similar composition (90).

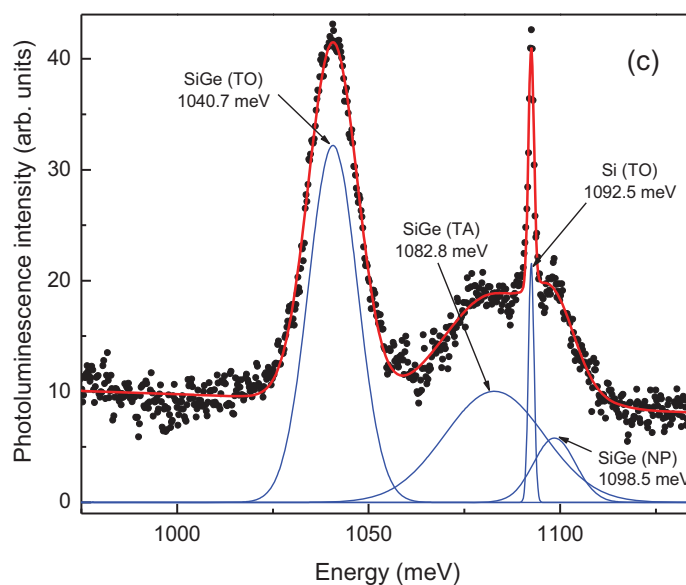


Figure 18. Curve-resolved PL spectrum of sample (C) at 25 K obtained with 405 nm excitation. The solid line shows the overall fit to the PL data, while the three SiGe NW component lines are shown beneath the fitted spectrum. The very sharp line at 1092.5 meV arises from the Si substrate.

From the fits to the sample with the strongest PL [sample (C)], the NW TA and TO phonon energies are found to be  $15.7 \pm 1.8$  and  $57.8 \pm 0.6$  meV, respectively, which agree very well with the values expected for bulk  $\text{Si}_{1-x}\text{Ge}_x$  with  $x = 0.15$  of  $18 \pm 1$  and 58 meV, respectively (90). The measured NW free-exciton NP energy of 1099 meV would indicate a Ge concentration of  $x = 0.14$  (giving an X-point energy gap of 1099 meV in bulk SiGe) (90). Thus the positions in energy of the NP peak and those of the accompanying phonon replicas independently confirm the alloy concentration as being  $x = 0.15 \pm 0.01$ .

In summary, the readily-observed PL arising from the SiGe NWs indicates they are clean (i.e., contain few growth defects and impurities) and are electrically isolated from the substrate. They are not strained to any significant extent and  $x$  for these samples is confirmed from the PL to be 0.15. These NWs with their well-controlled position, composition, and size and their efficient luminescence exhibit relevant features that are a significant improvement in quality over those produced by other vapor-solid-solid growth methods and that could be useful for applications in optoelectronic nanodevices. However, their mass production in current CMOS production lines would be problematic.

### Optical Emission from Germanium Nanocrystals

Previously, a very intense, low temperature PL with a long lifetime has been observed in numerous samples of MBE-grown  $\text{Si}_{1-x}\text{Ge}_x$  (SiGe) epitaxial layers with  $x$  ranging from 0.05 to 0.53 (113). Efficiencies in the 5% range – unheard of for group IV materials – were observed. This PL was neither defect nor dislocation related, and was suspected to be due to carrier localization effects. We have shown recently (114) that the PL is characteristic of self-assembled Ge nanocrystals (NCs) contained within the alloy epilayers through an investigation of its concentration dependence, both experimentally

and theoretically. The occurrence of these strained Ge NCs is confirmed through Raman spectroscopy measurements.

As can be seen in Fig. 19, the PL that we attribute to Ge NCs consists of a broad peak with an asymmetry to low photon energies. This peak displays little variation in shape with Ge-fraction and tracks the band gap (BG) variation, but is  $\sim 100$  meV below the indirect SiGe BG. If the material were Si or SiGe, the width of the peak at  $\sim 50$  meV would be too small for it to be due to a no-phonon (NP) line with its transverse-optic (TO) phonon replica, as the NP-TO spacing is about 58 meV for those materials. Figure 19 shows that for higher Ge-fractions the PL is emitted at energies significantly below those for bulk Ge, with its indirect BG of 744 meV at low temperatures. The origin of this broad, intense PL peak has remained unexplained, until now. In Fig. 19 we display low temperature PL from three SiGe samples and bulk Ge. For the spectrum in trace (a), the result is also illustrated with the results of curve fitting using two Gaussian peaks for the broad PL peak.

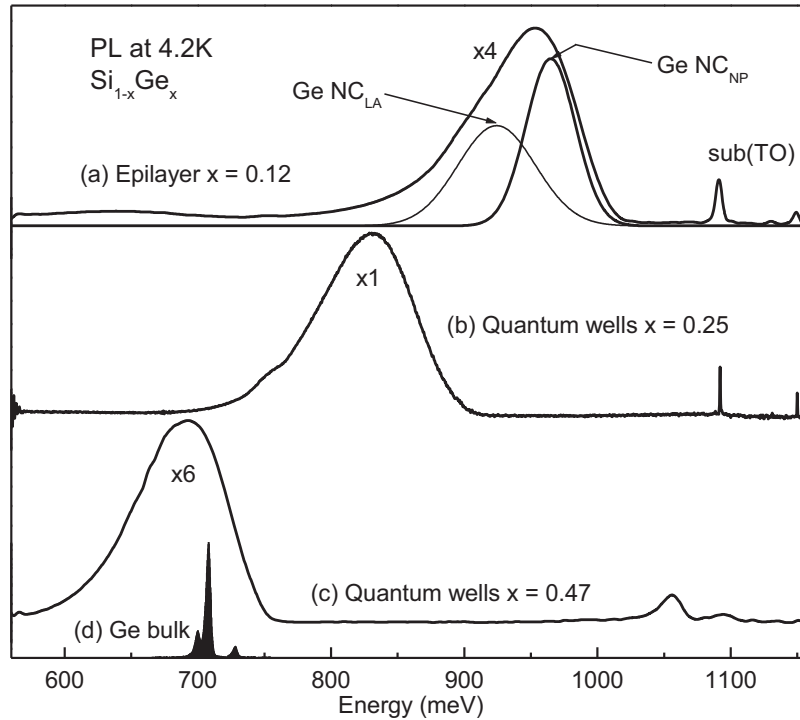


Figure 19. Low temperature PL from (a)-(c) three  $\text{Si}_{1-x}\text{Ge}_x$  samples and (d) bulk Ge. For the spectrum in trace (a), the result is also illustrated with curve fitting using two Gaussian peaks for the broad PL peak.

As is shown in Fig. 19(a), the broad peak's width and asymmetric shape can be curve-resolved into two symmetric peaks, separated by  $\sim 35$  meV, i.e., very near the momentum conserving TO phonon energy for Ge. The NP peak is wide (25-45 meV) due to NC confinement variations arising from size variability and to alloy disorder broadening in the SiGe. In Ge-dots, we expect two main PL peaks; a NP line and a longitudinal-acoustic (LA) phonon replica line, separated by about 28 meV. So the NP-phonon replica energies provided by curve resolving are relatively close to that (28 meV) for the most intense (LA) phonon replica for Ge, but differ very significantly from the

corresponding energy of the strongest (TO) phonon replica for Si and SiGe, which, in both cases, is 58 meV. We also notice inhomogeneous broadening due to size effects and that the NP peak is relatively large, as would occur for a high degree of carrier localization in Ge NCs.

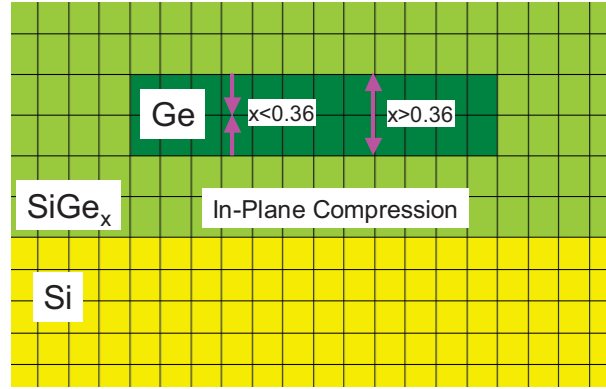


Figure 20. Cross-sectional schematic for the x-z plane of a lattice matched Ge NC within a Si<sub>1-x</sub>Ge<sub>x</sub> epilayer on Si(001).

An examination of the available experimental evidence indicates that a possible cause of the broad peak is imbedded Ge NCs within the SiGe layers (see Fig. 20). The formation of such NCs was shown in TEM studies (113) and by Raman spectroscopy (114). Referring to Fig. 20, we see that ideal epitaxial growth means that the SiGe epilayers and the Ge NCs be lattice matched to Si (001) in the x-y plane, so that both the SiGe and NCs are under compression in that plane. However, the growth of SiGe is unconstrained in the vertical (z) direction. As is well known, the SiGe epilayer is under tensile strain in this direction, leading to a vertical lattice constant that increases with Ge fraction and is larger than that for unstrained SiGe. Here the volume of the unit cell for the epitaxial SiGe layer is assumed to be the same as that for unstrained cubic (bulk) SiGe. An important assumption is that the lattice constant of the Ge NCs matches that of the SiGe in all three directions, i.e., including vertically. For relatively dilute SiGe, the Ge NCs are under compression vertically, but for increasing Ge-content in the SiGe epilayer the vertical lattice constant of the strained SiGe eventually exceeds that of bulk Ge. At the point where the vertical strain in the Ge NC first becomes tensile, the Ge-fraction in the SiGe is 0.36. With these constraints we can write down an expression for the strain in the z direction within the Ge NCs as:

$$\varepsilon_z = (c^{Ge} - c^{SiGez}) / c^{Ge} \quad [3]$$

where  $c^{Ge}$  is the bulk Ge lattice constant (5.658 Å) and  $c^{SiGez}$  is the strained lattice constant in the vertical direction for tetragonally distorted SiGe material, which is lattice matched to Si in the horizontal plane. Note that the strain value is negative for compression and positive for tension. With increasing  $x$ , this lattice constant varies from 5.431 to 6.141 Å as given by the following expression:

$$c^{SiGez} = (c^{SiGeu})^3 / (c^{Si})^2 \quad [4]$$

where  $c^{Si}$  is the lattice constant for Si (5.431 Å). Here  $c^{SiGeu}$  is the lattice constant for cubic (unstrained) SiGe given by:

$$c^{SiGeu} = c^{Si} + c_1x + c_2x^2 \quad [5]$$

where  $x$  is the Ge fraction. In this quadratic equation, the symbols  $c_1$  and  $c_2$  represent constants equal to 0.2 and 0.027, respectively (115). Strain versus Ge-fraction is thus easily derived for the vertical ( $z$ ) direction as shown by the horizontal scale at the bottom of the graph in Fig. 21.

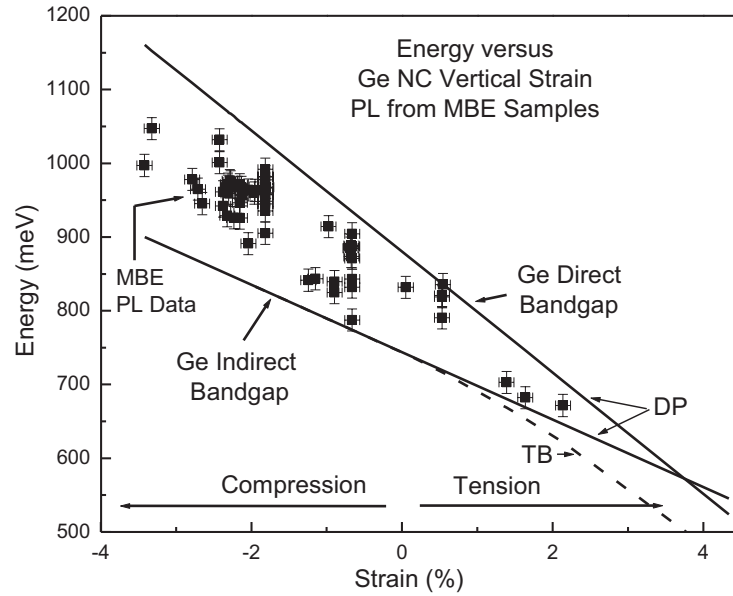


Figure 21. No-phonon line PL peak energy and bandgap (direct and indirect) energies of Ge versus Ge NC vertical strain. For the indirect gap under tensile strain, the energy has been calculated using the deformation potential (DP) and tight bonding (TB) theories.

Strain has a relatively large effect on the material bandgap energy, with compression generally increasing this energy while tension reduces it. A relatively simple method for calculating this effect is to use deformation potential (DP) theory, which employs linear relationships between strain and the direct and indirect bandgaps, as per:

$$E_{BG} = A + B\epsilon_z \quad [6]$$

Here, for strain expressed in per cent, the intercept and slope in the linear equation are 880 and -79.3 meV for the direct bandgap and 740 and -45.5 meV for the indirect one at low temperatures (116). For example, for a tensile strain of 2 %, the direct BG energy is 721 meV and the indirect BG is 649 meV.

From DP theory, as the strain becomes more strongly tensile both the direct and indirect gap energies decline, with the direct energy decreasing more rapidly than the indirect one. As shown in Fig. 21, the direct gap energy crosses over the indirect gap energy at a tensile uniaxial strain of 4 %, resulting in Ge becoming a direct gap semiconductor, a highly desirable outcome. Our results with PL point the way to this transition point, but the maximum vertical tensile strain for the present Ge NCs is not much greater than 2 %. Nonetheless, the fact that we see PL below the indirect BG of bulk Ge is explained by these particular Ge NCs being under tensile strain vertically, which reduces their Ge BG. There are other nonlinear models for the bandgap energy

such as the tight binding (TB) model (116), for which Fig. 21 contains the indirect bandgap calculation under tensile strain.

For the bandgap curves calculated versus strain in Fig. 21 the effects of quantum confinement have not been included. The data points were obtained by curve resolving the PL of the MBE-grown SiGe samples. In Fig. 21 the points are Ge NC NP PL peak energies and the solid lines are the direct and indirect NC BGs (Equation 6). The NP experimental peak energies have been obtained from the broad PL distributions by fitting Gaussian functions to the observed PL spectra. In Fig. 21 we note that the data falls generally above the indirect energy BG for uniaxially strained Ge, a differential which is most likely due to quantum confinement, as will be discussed next. This is a difference that appears to decrease as compression decreases, although there are only a few points for the larger tensile strains. The energy uncertainties in the data points are those obtained from curve resolving the PL peaks. The strain uncertainties for these points are derived from the X-ray diffraction measurements of the composition and thickness of the SiGe layers.

One point for discussion is whether or not quantum confinement for a reasonable range of NC sizes can account for the PL being at the energies above the strained bulk Ge indirect BG, as we see in Fig. 21. This difference is in the 50 to 150 meV range with an average of 103.4 meV. So we are asking whether such values are reasonable for quantum confinement effects in the Ge NCs. With the simple model described above we can provide an answer by calculating the size of the confinement effect versus NC size, quantum well thickness, and composition. In general it was found that the variation of NC confinement energy with thickness of the host SiGe was not that large ( $< 5$  meV) and the variation with Ge-fraction although larger was not a major contributor to the difference. For example, the NC confinement shift for a 1.5 nm NC in a 5 nm thick well was 110 meV for a Ge-fraction of 0.15 and 130 meV for a fraction of 0.50, everything else being equal. However, NC sizes in the range from 1 to 3 nm – corresponding to confinement energies from 120 to 50 meV – can indeed account for all the blue shifts from the predicted Ge NC BG that we see in the PL energies. This means that confinement shift provides a likely explanation for the difference seen between the measured PL energy and the NC bandgap and we estimate that the NC size varies from about 1 nm for a compressive strain of 4 % to 3 nm for tensile strain of 2 %.

The Raman spectroscopy results obtained from a representative set of samples were curve-fitted to obtain the various mode frequencies (114). The concentration dependence of the Ge-Ge (arising from the  $\text{Si}_{1-x}\text{Ge}_x$  alloy layer) and Ge (arising from the Ge NCs) mode frequencies are shown in Fig. 22. These data are consistent with the results of an earlier study (117). The existence of a sharp, although weak, Ge line in all spectra confirms the presence of Ge NCs in all of the samples studied by Raman spectroscopy. The approximately linear shift in frequency with  $x$  is a result of the strain in the alloy layer in the sample growth ( $z$ ) direction, which is the primary direction of phonon propagation sampled in the Raman back-scattering experiment.

From Chen et al. (118), the Ge-Ge phonon mode frequency  $\omega_{\text{Ge-Ge}}$  in  $\text{Si}_{1-x}\text{Ge}_x$ , as seen by Raman scattering, depends on the germanium fraction  $x$  and strain  $\varepsilon$  as follows:

$$\omega_{\text{Ge-Ge}} = 282.5 + 16x - 385\varepsilon. \quad [7]$$

For the Ge NCs,  $x$  is equal to unity. In the vertical direction the relevant strain,  $\varepsilon_z$ , for the NCs is given by Equation 3, leading to the red line in Fig. 22, in which the phonon frequency declines from 312 to 290  $\text{cm}^{-1}$  as  $x$  increases from 0.1 to 0.55. In the  $x$ - $y$  plane the NC strain is compressive and constant at -4.18 %, because the NCs are lattice matched to Si in this plane. Hence in the  $x$ - $y$  plane, the NC Raman frequency is not expected to vary with Ge fraction in the surrounding SiGe, as shown by the green horizontal line at a Raman frequency of 314.6  $\text{cm}^{-1}$  (calculated as per Equation 7) in Fig. 22.

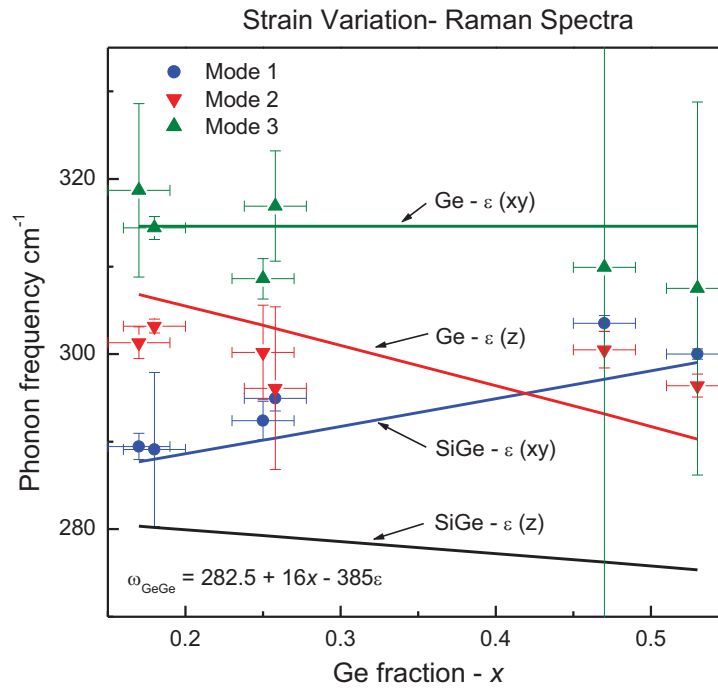


Figure 22. Concentration dependence of the zone-center Ge-Ge and Ge phonon mode frequencies, obtained from Raman scattering. For example, the blue points (●) correspond to a Ge-Ge mode in the  $\text{Si}_{1-x}\text{Ge}_x$ .

In the  $x$ - $y$  plane for the SiGe layers, the increasingly compressive strain causes the Ge-Ge Raman mode frequency to rise with Ge-fraction, as is apparent for the blue line in Fig. 22 for which the frequency goes up from 285 to 300  $\text{cm}^{-1}$  when the Ge-fraction changes from 0.1 to 0.55. In the vertical ( $z$ ) direction the strain is tensile in the SiGe layers and increases with Ge-fraction, which progressively suppresses the Ge-Ge phonon mode frequency, as seen in the black line below 280  $\text{cm}^{-1}$  in Fig. 22. The theoretical predictions are in general agreement with experiment, as can be seen in Fig. 22, which confirms our assignments and the presence of Ge NCs.

In conclusion, our modelling of the experimental results for the concentration dependence of the PL from strained  $\text{Si}_{1-x}\text{Ge}_x$  epilayers for  $0.05 < x < 0.55$  has shown that the intense PL at lower energies arises from imbedded Ge NCs. Such structures show promise for use as light emitters in device applications if appropriate growths at high  $x$  values can be engineered to introduce the predicted transition to a direct band gap within strained Ge NCs for  $x$ -values greater than 0.65.

## Other Nanostructures

A general overview of experimental and theoretical research into the optical properties of both crystalline and amorphous nanostructures formed from both Si and Ge has been given recently by Barbagiovanni *et al.* (112). Several of the most-recently-published papers providing new information in this field of research are profiled next.

### Germanium Light Sources

Germanium nanostructures have shown considerable promise for light emitting applications, as the indirect band gap of Ge can be converted to a direct one through a combination of applying tensile strain and appropriate doping at a high level [see, for example, the review of this field in Ref. (6)]. Although laser devices based on Ge have been demonstrated some time ago, at present there is no ability to produce such devices using complementary-metal-oxide-semiconductor (CMOS)-compatible processes (6). New information on the optical properties of strained Ge nanostructures has been obtained recently from fresh investigations of the intense broad PL produced by self-assembly during molecular beam epitaxy growth of strained  $\text{Si}_{1-x}\text{Ge}_x$  alloy layers on Si (113,114). A theory based on modelling the Ge nanostructures as quantum wires reproduces the observed energy shift of the PL and confirms that embedded Ge nanocrystals give rise to this light emission via carrier localization in three dimensions. By increasing the Ge-concentration of the alloy epilayer(s), the strain felt by the crystalline Ge nanostructures can be varied from compressive to tensile with the crossover occurring at  $x = 0.36$ . Such encapsulated Ge nanostructures are calculated to yield a direct band gap for  $x \geq 0.7$  and thus are good candidates for the production of a laser at near infrared wavelengths.

A different approach to obtaining bright light from Ge has been adopted by Moritz Brehm and co-workers (4,119–121). They have explored the properties of disordered-Ge quantum dots and found bright light emission at room temperature and even stimulated emission, much as was previously observed from disordered and crystalline Si quantum wells (51,86,122), but with the added advantage that the emission was at a desirable near infrared wavelength in the range 1.3–1.55  $\mu\text{m}$  rather than in the red for Si quantum wells. They have also demonstrated a light emitting diode based on their defect enhanced Ge quantum dots (121), which augers well for the integration of these light emitting nanostructures into conventional CMOS production lines.

Another novel approach towards improving the intensity of light emission from Ge dots is reported by Rutckaia *et al.* (123). Their method takes advantage of Mie resonances in specially constructed Si-based nanostructures, which involves coupling between the self-assembled Ge quantum dots and Si nanodisks. The near-infrared PL from an embedded dot is considerably enhanced due to a good spatial overlap between its physical position and the electric field of a Mie mode. Construction of structures containing nanodisk trimers resulted in a further 10-fold enhancement of the light emission. Such resonant dielectric nanostructures provide a new CMOS-compatible platform for the manipulation of light at the nanoscale.

In another ground-breaking piece of research, Amollo *et al.* (124) have explored the structural, optical, electronic and magnetic properties of reduced graphene oxide–Ge

quantum dot nanocomposites. Graphene has been of great interest recently for its applications in nanoelectronics and optoelectronics and this paper advances its use in developing nanocomposites for such applications. The functionalization of graphene was achieved via a single-step microwave-assisted solvothermal synthesis to produce the require nanocomposite structure containing quantum confined Ge ad-atoms on reduced graphene oxide sheets. The highly crystalline dots were spherical in shape and had diameters ranging from 1.6–9 nm. Optical spectroscopy revealed a clear dot size dependence of the light absorption in the ultraviolet region, strong and sharp PL at 380 nm in the ultraviolet, and a moderate intensity and broad emission at 450 nm with a tail extending across the visible wavelength region. These results are preliminary, but point to interesting possibilities in optoelectronics and the need for further research. From a device point of view, these composite nanostructures are readily dispersible in a polar solvent, which makes them appropriate for cost effective processing in solution.

The complexities of charge carrier behavior (creation, exchange, and recombination) in Ge quantum dots (dimensions: 14 nm across the base and 2.7 nm high) immersed in Si have been revealed in detail from a mid-infrared optical absorption study carried out by Vorobjev *et al.* (125). By measuring the variation in the optical transmission spectrum of the nanostructures under interband illumination, the authors have found that there is an increase of absorption at the long-wavelength edge of the spectrum, which ranges from 2–5  $\mu\text{m}$ , and a decrease of absorption at the short-wavelength edge. The increase of absorption is observed for light polarized along the growth direction and is related to the contribution of optical transitions involving non-equilibrium holes arising from the quantum dot ground state. The decrease of absorption at shorter wavelengths is observed for the same light polarization. This effect is proposed to be caused by the suppression of interband-like optical transitions between bound states in the valence and conduction bands and, interestingly, is essentially a *dynamic* analogue of the Burstein–Moss effect in bulk semiconductors. From an application point of view, it is useful to know that the optical transmittance variance related to non-equilibrium charge carriers becomes insignificant for temperatures greater than 250 K.

### Silicon Light Sources

Silicon nanostructures continue to be subjects of research with regards to improving their light emitting properties. Recent work by Vieira *et al.* (126) has extended earlier work on Si/SiO<sub>2</sub> multilayers (107) to investigate alloys of Ge with Si in the quantum wells, and, after high temperature annealing, thereby produce SiGe nanocrystals. By varying the alloy layer thickness from 2–3.5 nm, they were able to change the disposition of the alloy layer from isolated SiGe nanocrystals of 3–8 nm in size to a continuous layer of crystalline SiGe. However, only weak PL in the range 0.7–0.9 eV was observed from the nanocrystals at low temperature. The emission exhibited some structure that was associated with the presence of interface states between the crystalline nanostructures and the amorphous matrix surrounding them.

Investigations of the optical absorption of Si nanocrystals in single and multilayer structures where the nanocrystals were confined between variable thickness SiO<sub>2</sub> barrier layers have been carried out by Greben *et al.* (127). The absorption cross-section was determined as a function of barrier thickness by using a PL modulation method. A large variation of the absorption strength with barrier layer thickness was observed and

explained as a consequence of the efficiency of energy transfer between the layers of Si nanocrystals and/or defect population states. Such information is important when designing structures containing Si nanocrystals for use in next-generation Si-photonics and Si voltaic devices.

Recent theoretical (128) and experimental (128,129) work on the optical properties of Si nanocrystals has shed more light on the emission mechanisms involved in earlier observations reported in 2010 of a red spectral shift and enhanced quantum efficiency in phonon-free PL from silicon nanocrystals (130). In the News and Views Section of the same issue of *Nature Nanotechnology* as Ref. (130), Kovalev wrote “Can silicon ever be a true direct-bandgap semiconductor? The first observation of a new, short-lived PL band from silicon nanocrystals offers fresh hope.” (131), which raised expectations for new applications of Si nanocrystals within Si optoelectronics. The new theoretical and experimental work of Ref. (128), however, has cast doubt on the interpretation of the original experimental work (130). Luo *et al.* (128) suggest that state filling assisted by strong pumping with subsequent fast recombination of multi-excitons could be responsible for the red-shifted emission, as higher states are emptied faster for smaller nanocrystals. Consequently, the very fast recombination observed in Ref. (130) could be attributed to multi-exciton or Auger recombination, and thus is not the highly-desired direct-band transition. In reply, de Boer *et al.* (129), after reviewing a number of different aspects of the work of Luo *et al.* (128) and other related works, assert that Luo *et al.* have not untangled the mystery of source of the red-shift in band energy. They think that the results of Luo *et al.*'s modelling actually support their previous assignment of the fast PL band as arising from the  $\Gamma$ -valley character admixture within Si-nanocrystals into states with energies below the bulk-Si direct band gap. Clearly, more experimental and theoretical work on this topic is necessary before proceeding with any technological applications requiring use of a direct band gap in Si nanocrystals.

### Conclusion

The development of a light emitter compatible with Si based CMOS circuit technology and fast optical interconnects is very important for the upcoming generations of microprocessors and computers. Self-assembled Si, Ge, and SiGe nanostructures with light emission in the all-important optical communication wavelength range of 1.3–1.55  $\mu\text{m}$  are compatible with conventional CMOS processes and, based on present results obtained with specially engineered structures, are also able to produce the requisite fast emission times. The wide variety of new bright sources of PL considered here are promising, but not yet ready for applications, and require further research and development work. At present, it appears that strained Ge nanostructures are the most promising ones for the near-infrared lasers needed urgently for their compatibility with fiber optics.

### Acknowledgments

This paper has been based on material covered in my Gordon E. Moore Medal Address at the ECS Spring 2019 Meeting held in Dallas, Texas. I am very grateful to the ECS for recognizing our work with this award, to the National Research Council Canada for their foresight in allowing this research to proceed for more than three decades, and to my many colleagues there for their support. Some of the results summarized here have

been published elsewhere in greater detail in Refs. (8–12,89,114). This particular work has been carried out in extensive collaborations here at the National Research Council, Ottawa, Canada with primarily Drs. J.-M. Baribeau, J. P. McCaffrey, N. L. Rowell, and X. Wu; and with the research groups of Professor L. Tsybeskov, New Jersey Institute of Technology, Newark, New Jersey, USA and Professor I. Berbezier, Institut Matériaux Microélectronique Nanosciences de Provence, Marseille, France. I am grateful for the many contributions of these and my many other colleagues to this joint work.

### References

1. D. J. Lockwood, Ed., *Light Emission in Silicon*, Academic Press, New York (1998).
2. J.-M. Baribeau, X. Wu, N.L. Rowell, and D.J. Lockwood, *J. Phys.: Condens. Matter* **18**, R139 (2006).
3. J.-N. Aqua, I. Berbezier, L. Favre, T. Frisch, and A. Ronda, *Phys. Reports* **522**(2), 59 (2013).
4. M. Brehm and M. Grydlik, *Nanotechnology* **28**, 392001 (2017).
5. L. Pavesi and D. J. Lockwood, Eds., *Silicon Photonics*, Springer, Berlin (2004).
6. S. Saito, A. Z. Al-Attili, K. Oda, and Y. Ishikawa, *Semicond. Sci. Technol.* **31**, 043002 (2016).
7. D. J. Lockwood and L. Tsybeskov, *IEEE J. Sel. Top. Quantum Electronics* **20**(4), 8200807 (2014).
8. D. J. Lockwood, N. L. Rowell, A. Gouyé, L. Favre, A. Ronda, and I. Berbezier, *ECS Trans.* **61**(5), 31 (2014).
9. S. A. Mala, L. Tsybeskov D. J. Lockwood, X. Wu, and J.-M. Baribeau, *Appl. Phys. Lett.* **103**, 033103 (2013).
10. S. A. Mala, L. Tsybeskov, D. J. Lockwood, X. Wu, and J.-M. Baribeau, *Physica B* **453**, 29 (2014).
11. A. Benkouider, A. Ronda, A. Gouye, C. Herrier, L. Favre, D. J. Lockwood, N. L. Rowell, A. Delobbe, P. Sudraud, and I. Berbezier, *Nanotechnology* **25**(33), 335303 (2014).
12. D. J. Lockwood, N. L. Rowell, A. Benkouider, A. Ronda, L. Favre, and I. Berbezier, *Beilstein J. Nanotechnol.* **2014**(5), 2498 (2014).
13. A. Uhlir, *Bell Syst. Tech. J.* **35**, 333 (1956).
14. D. R. Turner, *J. Electrochem. Soc.* **105**, 402 (1958).
15. T. Unagami and M. Seki, *J. Electrochem. Soc.* **125**, 1339 (1978).
16. M. I. J. Beale, J. D. Benjamin, M. J. Uren, N. G. Chew, and A.G. Cullis, *J. Cryst. Growth* **73**, 622 (1985).
17. G. Bomchil, A. Halimaoui, and R. Herino, *Appl. Surf. Sci.* **41-42**, 604 (1990).
18. M. I. J. Beale, N. G. Chew, M. J. Uren, A. G. Cullis, and J. D. Benjamin, *Appl. Phys. Lett.* **46**, 86 (1985).
19. K. Barla, R. Herino, G. Bomchil, J. C. Pfister, and A. Freund, *J. Cryst. Growth* **69**, 726 (1984).
20. Y. Watanabe, Y. Arita, T. Yokoyama, and Y. Igarashi, *J. Electrochem. Soc.* **122**, 1351 (1975).
21. K. Imai, *Sol. State Electron.* **24**, 159 (1981).
22. C. Pickering, M. I. J. Beale, D. J. Robbins, P. J. Pearson, and R. Greef, *J. Phys. C* **17**, 6535 (1984).
23. L.T. Canham, *Phys. World* **5**(3), 41 (1992).

24. L.T. Canham, *Appl. Phys. Lett.* **57**, 1046 (1990).
25. A.G. Cullis and L.T. Canham, *Nature* **353**, 335 (1991).
26. V. Lehmann and U. Gösele, *Appl. Phys. Lett.* **58** 856 (1991).
27. D. J. Lockwood, *Solid State Commun.* **92**, 101 (1994).
28. D. J. Lockwood, G. C. Aers, L. B. Allard, B. Bryskiewicz, S. Charbonneau, D. C. Houghton, J. P. McCaffrey, and A. Wang, *Can. J. Phys.* **70**, 1184 (1992).
29. D. J. Lockwood, A. Wang, and B. Bryskiewicz, *Solid State Commun.* **89**, 587 (1994).
30. D.J. Lockwood, A.G. Wang and B. Bryskiewicz, in *Quantum Confinement: Physics and Applications*, M. Cahay, S. Bandyopadhyay, J. P. Leburton, A. W. Kleinsasser, and M. A. Osman, Eds., p. 222, Electrochem. Soc., Pennington, NJ, (1994).
31. R. Siegele, H. K. Haugen, D. J. Lockwood, B. Bryskiewicz, J. F. Forster, and H. R. Andrews, *Solid State Commun.* **93**, 833 (1995).
32. D. J. Lockwood and A.G. Wang, *Solid State Commun.* **94**, 905 (1995).
33. P. Schmuki, L. E. Erickson, and D. J. Lockwood, *Phys. Rev. Lett.* **80**, 4060 (1998).
34. J.R. Proot, C. Delerue, and G. Allan, *Appl. Phys. Lett.* **61**, 1948 (1992).
35. T. Takagahara and K. Takeda, *Phys. Rev. B* **46**, 15578 (1992).
36. M. S. Hybertsen, *Phys. Rev. Lett.* **72**, 1514 (1994).
37. Y. Kanemitsu, H. Uto, Y. Masumoto, T. Matsumoto, T. Futagi, and H. Mimura, *Phys. Rev. B* **48**, 2827 (1993).
38. S. Furukawa and T. Miyasato, *Phys. Rev. B* **38**, 5726 (1988).
39. C. Delerue, G. Allan, and M. Lannoo, *Phys. Rev. B* **48**, 11024 (1993).
40. M. V. Wolkin, J. Lorne, P. M. Fauchet, G.Allan, and C. Delerue, *Phys. Rev. Lett.* **82**, 197 (1999).
41. R. Boukherroub, S. Morin, D. D. M. Wayner, and D. J. Lockwood, *Phys. Stat. Sol. (a)*, **182**, 117 (2000).
42. R. Boukherroub, S. Morin, D. D. M. Wayner, F. Bensebba, G. I. Sproule, J.-M. Baribeau, and D. J. Lockwood, *Chem. Mater.* **13**, 2002 (2001).
43. R. Boukherroub, D. D. M. Wayner, D. J. Lockwood, and L. T. Canham, *J. Electrochem. Soc.* **148**, H91 (2001).
44. R. Boukherroub, J. T. C. Wojtyk, D. D. M. Wayner, and D. J. Lockwood, *J. Electrochem. Soc.* **149**, H59 (2002).
45. R. Boukherroub, D.D.M. Wayner and D.J. Lockwood, *Appl. Phys. Lett.* **81**, 601 (2002).
46. B. Gelloz, H. Sano, R. Boukherroub, D. D. M. Wayner, D. J. Lockwood, and N. Koshida, *Appl. Phys. Lett.* **83**, 2342 (2003).
47. R. Tsu, *Nature* **364**, 19 (1993).
48. C. J. Frosch and L. Derick, *J. Electrochem. Soc.* **104**, 547 (1957).
49. D. J. Lockwood, *Phase Transitions* **68**, 151 (1999).
50. Z. H. Lu, D. J. Lockwood, and J.-M. Baribeau, *Nature* **378**, 258 (1995).
51. D. J. Lockwood, Z. H. Lu, and J.-M. Baribeau, *Phys. Rev. Lett.* **76**, 539 (1996).
52. A. Zunger and L.-W. Wang: *Appl. Surf. Sci.* **102**, 350 (1996).
53. Z. H. Lu, D. J. Lockwood, and J.-M. Baribeau, *Solid-State Electron.* **40**, 197 (1996).
54. R. Tsu, A. Filios, C. Lofgren, K. Dovidenko, and C. G. Waugh, *Electrochem. Solid-State Lett.* **1**, 80 (1998).
55. D. J. Lockwood, J.-M. Baribeau, and Z. H. Lu, in *Advanced Luminescent Materials*, D. J. Lockwood, P. M. Fauchet, N. Koshida, and S. R. J. Brueck, Eds., p. 339, The Electrochemical Society Proceedings Series, Pennington, NJ (1996).

56. J. A. Brum and G. Bastard, *J. Phys. C. Solid State Phys.* **18**, L789 (1985).
57. Z. H. Lu, J.-M. Baribeau, D. J. Lockwood, M. Buchanan, N. Tit, C. Dharma-wardana, and G. C. Aers, *SPIE Proc.* **3491**, 457 (1998).
58. B. T. Sullivan, D. J. Lockwood, H. J. Labbé, and Z.-H. Lu, *Appl. Phys. Lett.* **69**, 3149 (1996).
59. D. J. Lockwood, B. T. Sullivan, and H. J. Labbé, *J. Lumin.* **80**, 75 (1999).
60. D. J. Lockwood and L. Tsybeskov, *J. Nanophotonics* **2**, 022501 (2008).
61. R. Tsu, Q. Zhang, and A. Filios, *SPIE Proc.* **3290**, 246 (1997).
62. A. G. Nassiopoulou, V. Ioannou-Sougleridis, P. Photopoulos, A. Travlos, V. Tsakiri, and D. Papadimitriou, *Phys. Stat. Sol. (a)* **165**, 79 (1998).
63. G. G. Qin, S. Y. Ma, Z. C. Ma, W. H. Zong, and L. P. You, *Solid State Commun.* **106**, 329 (1998).
64. L. Heikkilä, T. Kuusela, H.-P. Hedman, and H. Ihanola, *Appl. Surf. Sci.* **133**, 84 (1998).
65. V. Ioannou-Sougleridis, V. Tsakiri, A. G. Nassiopoulou, P. Photopoulos, F. Bassani, and F. Arnaud d'Avitaya, *Phys. Stat. Sol. (a)* **165**, 97 (1998).
66. M. Zacharias and P. Streitenberger, *Phys. Rev. B* **62**, 8391 (2000).
67. Y. Takahashi, T. Furuta, Y. Ohno, T. Ishiyama, and M. Tabe, *Jpn. J. Appl. Phys.* **34**, 950 (1995).
68. Y. Kanemitsu and S. Okamoto, *Phys. Rev. B* **56**, R15561 (1997).
69. E.-C. Cho, M. A. Green, R. Corkish, P. Reece, M. Gal, and S.-H. Lee, *J. Appl. Phys.* **101**, 063105 (2007).
70. Z. H. Lu and D. Grozea, *Appl. Phys. Lett.* **80**, 255 (2002).
71. N. Sato and T. Yonehara, *Appl. Phys. Lett.* **65**, 1924 (1994).
72. Z. H. Lu, J.-M. Baribeau and D. J. Lockwood, *J. Appl. Phys.* **76**, 3911 (1994).
73. D. J. Lockwood, Z. H. Lu, and D. Grozea, in *Advanced Luminescent Materials and Quantum Confinement II*, M. Cahay, J. P. Leburton, D. J. Lockwood, S. Bandyopadhyay, N. Koshida, and M. Zacharias, Eds., p. 159, The Electrochemical Society Proceedings Series, Pennington, NJ (2002).
74. D. J. Lockwood, Z. H. Lu and D. Grozea, *SPIE Proc.* **4808**, 40 (2002).
75. D. J. Lockwood, Z. H. Lu and D. Grozea, *Inst. Phys. Conf. Series* **171**, G3.1 (2003).
76. D. J. Lockwood, M. W. C. Dharma-wardana, Z. H. Lu, D. H. Grozea, P. Carrier and L. J. Lewis, *Mat. Res. Soc. Proc.* **737**, 243 (2003).
77. D. J. Lockwood, R. L. Williams and Z.-H. Lu, in *Nanoscale Devices, Materials, and Biological Systems: Fundamentals and Applications*, M. Cahay, M. Urquidi-Macdonald, S. Bandyopadhyay, P. Guo, H. Hasegawa, N. Koshida, J. P. Leburton, D. J. Lockwood, S. Seal and A. Stella, Editors, p. 243, The Electrochemical Society Proceedings Series, Pennington, NJ (2005).
78. B. K. Agrawal and S. Agrawal, *Appl. Phys. Lett.* **77**, 3039 (2000).
79. P. Carrier, L. J. Lewis, and M. W. C. Dharma-wardana, *Phys. Rev. B* **65**, 165339 (2002).
80. C. Delerue, G. Allan, and M. Lannoo, in *Light Emission in Silicon*, D. J. Lockwood, Ed., Chapter 7, Academic Press, New York (1998).
81. I. Vasiliev, S. Ogut, and J. R. Chelikowsky, *Phys. Rev. B* **65**, 115416 (2002).
82. S. Zollner, D. J. Lockwood, and Z. H. Lu (private communication).
83. D. J. Lockwood, in *Light Emission in Silicon*, D. J. Lockwood, Ed., Academic Press, New York (1998).

84. Y. Kanemitsu, in *Light Emission in Silicon*, D. J. Lockwood, Ed., Chapter 5, Academic Press, New York (1998).
85. S. Saito, D. Hisamoto, H. Shimizu, H. Hamamura, R. Tsuchiya, Y. Matsui, T. Mine, T. Arai, N. Sugii, K. Torii, S. Kimura, and T. Onai, *Appl. Phys. Lett.* **89**, 163504 (2006).
86. S. Saito, Y. Suwa, H. Arimoto, N. Sakuma, D. Hisamoto, H. Uchiyama, J. Yamamoto, T. Sakamizu, T. Mine, S. Kimura, T. Sugawara, and M. Aoki, *Appl. Phys. Lett.* **95**, 241101 (2009).
87. M. d'Avezac, J.-W. Luo, T. Chanier, and A. Zunger, *Phys. Rev. Lett.* **108**, 027401 (2012).
88. H. J. Xiang, B. Huang, E. Kan, S.-H. Wei, and X. G. Gong, *Phys. Rev. Lett.* **110**, 118702 (2013).
89. D. J. Lockwood, N. L. Rowell, L. Favre, A. Ronda and I. Berbezier, *ECS J. Solid State Sci. Tech.*, **7**(8), R115 (2018).
90. J. Weber and M. I. Alonso, *Phys. Rev. B* **40**, 5683 (1989).
91. R. Sauer, J. Weber, J. Stolz, E. R. Weber, K.-H. Kfisters, and H. Alexander, *Appl. Phys. A* **36**, 1 (1985).
92. W. M. Duncan, P.-H. Chang, B.-Y. Mao, and C.-E. Chen, *Appl. Phys. Lett.* **51**, 773 (1987).
93. G. Davies, *Phys. Reports* **176**, 83 (1989).
94. S. Fukatsu, Y. Mera, M. Inoue, K. Maeda, H. Akiyama, and H. Sakaki, *Appl. Phys. Lett.* **68**, 1889 (1996).
95. N. L. Rowell, J.-M. Baribeau, and D. C. Houghton, in *Proceedings of the Second International Symposium on Silicon Molecular Beam Epitaxy*, J. C. Bean and L. J. Schowalter, Eds., p. 48, *Electrochem. Soc. Proc.*, **88**(8), (1988).
96. D. J. Lockwood and L. Tsybeskov, in *Handbook of Silicon Photonics*, L. Vivien and L. Pavesi, Eds., pp. 354-371, CRC Press, Boca Raton, FL (2013).
97. N. Modi, D. J. Lockwood, J.-M. Baribeau, X. Wu, and L. Tsybeskov, *J. Appl. Phys.* **111**, 114313 (2012).
98. B. V. Kamenev, L. Tsybeskov, J.-M. Baribeau, and D. J. Lockwood, *Phys. Rev. B* **72**, 193306 (2005).
99. B. V. Kamenev, L. Tsybeskov, J.-M. Baribeau, and D. J. Lockwood, *Appl. Phys. Lett.*, **84**, 1293 (2004).
100. E.-K. Lee, D. J. Lockwood, J.-M. Baribeau, A. M. Bratkovsky, T. I. Kamins, and L. Tsybeskov, *Phys. Rev. B* **79**, 233307 (2009).
101. B. Ohnesorge, M. Albrecht, J. Oshinowo, A. Forchel, and Y. Arakawa, *Phys. Rev. B* **54**, 11532 (1996).
102. S. Fukatsu, Y. Mera, M. Inoue, K. Maeda, H. Akiyama, and H. Sakaki, *Appl. Phys. Lett.* **68** (1996).
103. A. Zrenner, B. Fröhlich, J. Brunner, and G. Abstreiter, *Phys. Rev. B* **52**, 16608 (1995).
104. I. Kuskovsky, G. F. Neumark, V. N. Bondarev, and P. V. Pikhitsa, *Phys. Rev. Lett.* **80**, 2413 (1998).
105. D. G. Thomas, J. J. Hopfield, and W. M. Augustyniak, *Phys. Rev.* **140**, A202 (1965).
106. J. Xiang, W. Lu, Y. Hu, Y. Wu, H. Yan, and C. M. Lieber, *Nature* **441**, 489 (2006).
107. G. Conibeer, M. Green, R. Corkish, Y. Cho, E. C. Cho, C. W. Jiang, T. Fangsuwannarak, E. Pink, Y. D. Huang, T. Puzzer, T. Trupke, B. Richards, A. Shalav, and K. L. Lin, *Thin Solid Films* **511**, 654 (2006).

108. P. Werner, N. D. Zakharova, G. Gertha, L. Schuberta, and U. Gösele, *Int. J. Mat. Res.* **97**(7), 1008 (2006).
109. E. Sutter, B. Ozturk, and P. Sutter, *Nanotechnology* **19**, 435607 (2008).
110. J. P. Noel, N. L. Rowell, and J. E. Greene, *J. Appl. Phys.* **77**, 4623 (1995).
111. Y. S. Tang, C. D. Wilkinson, C. M. Sotomayor Torres, D. W. Smith, T. E. Whall, and E. H. C. Parker, *Solid State Commun.* **85**, 199 (1993).
112. E. G. Barbagiovanni, D. J. Lockwood, P. J. Simpson, and L. V. Goncharova, *Appl. Phys. Rev.* **1**(1), 011302 (2014).
113. N. L. Rowell, J.-P. Noël, D. C. Houghton, A. Wang, L. C. Lenchyshyn, M. L. W. Thewalt, and D. D. Perovic, *J. Appl. Phys.*, **74**, 2790 (1993).
114. N. L. Rowell, D. J. Lockwood, D. C. Houghton, J.-P. Noël, and J.-M. Baribeau, *ECS J. Solid State Sci. Tech.* **7**(12), R195 (2018).
115. J. P. Dismukes, L. Ekstrom and R. J. Paff, *J. Phys. Chem.* **68**, 3021 (1964).
116. K. Guilloy, N. Pauc, A. Gassenq, Y. M. Niquet, J. M. Escalante, I. Duchemin, S. Tardif, G. Osvaldo Dias, D. Rouchon, J. Widiez, J. M. Hartmann, R. Geiger, T. Zabel, H. Sigg, J. Faist, A. Chelnokov, V. Reboud, and V. Calvo, *ACS Photonics* **3**, 1907 (2016).
117. H. K. Shin, D. J. Lockwood, and J. M. Baribeau, *Solid State Commun.* **114**, 505 (2000).
118. H. Chen, Y. K. Li, C. S. Peng, H. F. Liu, Y. L. Liu, Q. Huang, J. M. Zhou, and Qi-Kun Xue, *Phys. Rev. B* **65**, 233303 (2002).
119. M. Grydlik, F. Hackl, H. Groiss, M. Glaser, A. Halilovic, T. Fromherz, W. Jantsch, F. Schäffler, and M. Brehm, *ACS Photonics* **3**, 298 (2016).
120. M. Grydlik, M. T. Lusk, F. Hackl, A. Polimeni, T. Fromherz, W. Jantsch, F. Schäffler, and M. Brehm, *Nano Lett.* **16**, 6802 (2016).
121. P. Rauter, L. Spindlberger, F. Schäffler, T. Fromherz, J. Freund, and M. Brehm, *ACS Photonics* **5**(2), 431 (2017).
122. D. J. Lockwood, *ECS Trans.* **50**(37), 39 (2013).
123. V. Rutckaia, F. Heyroth, A. Novikov, M. Shaleev, M. Petrov, and J. Schilling, *Nano Lett.* **17**, 6886 (2017).
124. T. A. Amollo, G. T. Mola, and V. O. Nyamori, *Nanotechnology* **28**, 495703 (2017).
125. L. E. Vorobjev, D. A. Firsov, V. Yu Panevin, A. N. Sofronov, R. M. Balagula, and A. A. Tonkikh, *J. Phys: Conf. Series* **586**, 012001 (2015).
126. E. M. F. Vieira, J. Toudert, A. G. Rolo, A. Parisini, J. P. Leitão, M. R. Correia, N. Franco, E. Alves, A. Chahboun, J. Martín-Sánchez, R. Serna, and M. J. M. Gomes, *Nanotechnology* **28**, 345701 (2017).
127. M. Greben, P. Khoroshyy, S. Gutsch, D. Hiller, M. Zacharias, and J. Valenta, *Beilstein J. Nanotechnol.* **2017**(8), 2315 (2017).
128. J.-W. Luo, S.-S. Li, I. Sychugov, F. Pevero, J. Linnros, and A. Zunger, *Nature Nanotech.* **12**, 930 (2017).
129. W. de Boer, D. Timmerman, I. Yassievich, A. Capretti, and T. Gregorkiewicz, *Nature Nanotech.* **12**, 932 (2017).
130. W. D. A. M. de Boer, D. Timmerman, K. Dohnalová, I. N. Yassievich, H. Zhang, W. J. Buma, and T. Gregorkiewicz, *Nature Nanotech.* **5**, 878 (2010).
131. D. Kovalev, *Nature Nanotech.* **5**, 827 (2010).